Non-Abelian Reciprocal Braiding of Weyl Nodes

Adrien Bouhon[1,2],* Robert-Jan Slager[3],† and Tomáš Bzdušek[4,5]‡
[1] *Department of Physics and Astronomy, Uppsala University, Box 516, SE-751 21 Uppsala, Sweden*
[2] *Nordic Institute for Theoretical Physics (NORDITA), Stockholm, Sweden*
[3] *Department of Physics, Harvard University, Cambridge, MA 02138*
[4] *Department of Physics, McCullough Building, Stanford University, Stanford, CA 94305, USA and*
[5] *Stanford Center for Topological Quantum Physics, Stanford University, Stanford, CA 94305, USA*
(Dated: October 22, 2019)

We illustrate a procedure that defines and converts non-Abelian charges of Weyl nodes via braid phase factors, which arise upon exchange inside the reciprocal momentum space. This phenomenon derives from intrinsic symmetry properties of topological materials, which are increasingly becoming available due to recent cataloguing insights. Specifically, we demonstrate that band nodes in systems with $C_2\mathcal{T}$ symmetry exhibit such braiding properties, requiring no particular fine-tuning. We further present observables in the form of generalized Berry phases, calculated via a mathematical object known as Euler form. We demonstrate our findings with explicit models and a protocol involving three bands, for which the braid factors mimic quaternion charges. This protocol is implementable in cold atoms setups and in photonic systems, where observing the proposed braid factors relates to readily available experimental techniques. The required $C_2\mathcal{T}$ symmetry is also omnipresent in graphene van-der-Waals heterostructures, which might provide an alternative route towards realizing the non-Abelian conversion of band nodes.

Topological phases of matter constitute one of the most active research areas in physics. The robust and illustrious properties of intrinsic topological order, such as protected edge states and the possibility of excitations that exhibit non-trivial braiding statistics [1], open up routes to potentially translate mathematical understanding of physical phenomena to new generations of quantum technology. This has arguably also fuelled the discovery of topological band structures [2, 3] that can effectively give rise to such physical features [2–4]. The past decade has witnessed considerable progress in cataloguing topological materials [5–16], thereby providing an increasingly viable platform for bringing the potential of topological materials to experiment.

In this work, we report a concrete protocol that elucidates a novel physical phenomenon, which naturally arises from the interplay of symmetry and topology in metals and semimetals. More concretely, we show that in systems having $C_2\mathcal{T}$ symmetry, i.e. a composition of time reversal with a π-rotation, band degeneracies (so-called "nodes") are characterized by non-Abelian topological charges. The values of these charges can be converted via non-trivial phase factors, which arise upon braiding the nodes inside the reciprocal momentum space. We discuss how the conversion effect can be exposed using generalized Berry phases, which we formulate using a mathematical quantity known as Euler form. Besides uncovering the underlying mathematical structures, inspired by insights from the physics of nematic liquids, we also relate our theoretical predictions to experimentally viable settings. In particular, we introduce a two-dimensional three-band model, which is directly implementable in cold-atom and photonic systems. Most importantly, we also uncover three-dimensional generalizations, and discuss possible experimental realizations in van-der-Waals heterostructures.

Three band model and braiding protocol.— We find that the ability of band nodes to pairwise annihilate crucially depends on the presence of band nodes in other band gaps. This enables non-trivial braiding of band nodes inside the reciprocal momentum ($\boldsymbol{k}$) space, as illustrated in Fig. 1**a**–**b**. For the sake of simplicity, we explicitly consider three-band models, and we introduce the following terminology. The main gap of interest, hosting the Fermi level, is called "principal gap". Accordingly, band nodes in this gap will be referred to as "principal nodes". The other band gap, as well as the corresponding band and nodes, are designated as "adjacent".

To make our study concrete, we consider the Hamiltonian with a single tuning parameter t,

$$H(\boldsymbol{k};t)=\begin{pmatrix} f(t) & g(\boldsymbol{k}) & g^*(\boldsymbol{k}) \\ g^*(\boldsymbol{k}) & 0 & h(\boldsymbol{k};t) \\ g(\boldsymbol{k}) & h^*(\boldsymbol{k};t) & 0 \end{pmatrix} \tag{1}$$

with the onsite energy $f(t)=F_{[8,-]}(t)$, the couplings $g(\boldsymbol{k})=-\mathrm{i}(\mathrm{e}^{-\mathrm{i}k_1\pi}-\mathrm{e}^{-\mathrm{i}k_2\pi})$ and $h(\boldsymbol{k};t)=h_0(t)+h_1(t)(\mathrm{e}^{\mathrm{i}k_1\pi}+\mathrm{e}^{\mathrm{i}k_2\pi})$ with $h_0(t)=F_{[2,-]}(t)$ and $h_1(t)=[10-F_{[8,+]}(t)]$. The dependence on the control parameter $t\in[-10,10]$ is defined through $F_{[\nu,\pm]}(t)=\frac{1}{2}\left(|t+\nu|\pm|t-\nu|\right)$, which is a piecewise-linear function with shoulders at $+\nu$ and at $-\nu$, see Fig. 2**a**. The practical implementation of the model in Eq. (1) requires the ability to tune only three

* adrien.bouhon@su.se
† robertjanslager@fas.harvard.edu
‡ bzdusek@stanford.edu

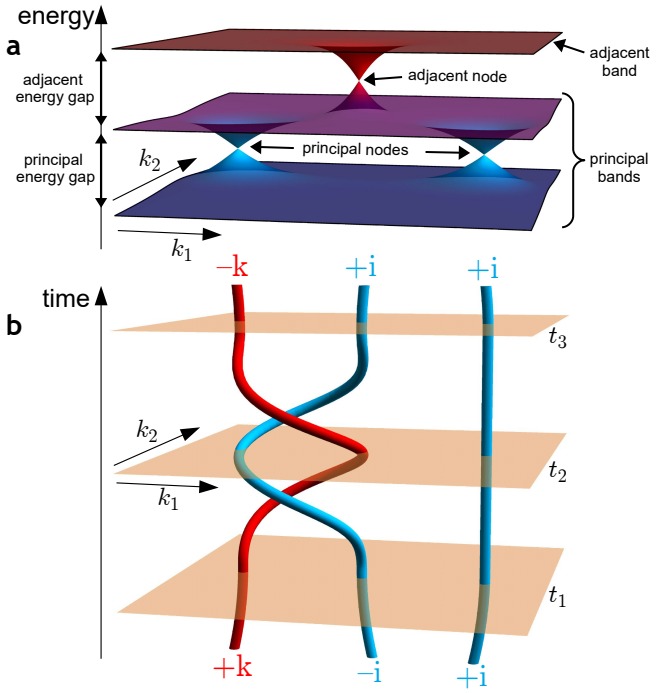

FIG. 1. **Non-trivial exchange of band nodes. a.** Summary of the terminology introduced in the text. We investigate the capability of the "principal" nodes, assumed to be near the Fermi level, to pairwise annihilate. We consider two "principal" bands that form nodal points (blue), and a third "adjacent" band which enables additional species of band nodes (red) formed among the unoccupied bands. **b.** By adjusting the Hamiltonian parameters as a function of time (orange planes $t_{1,2,3}$), the node trajectories can form non-trivial braids inside the reciprocal momentum (k_1, k_2) space. Such an exchange of nodes converts their topological charges, indicated by quaternion numbers $\pm$i and $\pm$k, and affects the capability of the nodes to pairwise annihilate. Note that the band structure in panel (a) corresponds to the situation in panel (b) at time t_2.

tight-binding parameters, namely the potential on the first site, and the hopping amplitude between the latter two sites along the horizontal resp. vertical direction. The physical degrees of freedom $\{\phi_\alpha\}_{\alpha=A,B,C}$ are three s-wave orbitals, fulfilling $\phi_C = C_2\phi_B$, where the C_2 rotation axis is taken perpendicularly to the basal plane [17]. The model breaks C_2 and $\mathcal{T}$ but preserves the combined anti-unitary symmetry $C_2\mathcal{T}$.

We realize the centre braiding protocol by increasing the adiabatic control parameter ("time") t in Eq. (1) from -10 to 10. By construction, the model exhibits nodal points only along the two diagonals of the Brillouin zone, $(1\bar{1})$ and (11), connecting Γ and M. In Fig. 2**c**, we show snaphots of the band structure along these diagonals during the braiding protocol with solid resp. dashed cruves. The orange arrows in the same panel indicate the motion of the nodal points upon increasing time. Furthermore, Fig. 2**d** displays the configuration of the nodal points over the 2D Brillouin zone at a few matching times, and keeps track of their past trajectory.

At the initial time $t=-10$, the three bands are gapped. At $t=-8$, the adjacent gap exhibits a pair of nodal points moving from Γ (where they were created) towards M along $(1\bar{1})$. At $t=-4$, there are two principal nodes moving from M (where they were created) towards Γ along (11). At $t=-2$, the principal nodes meet at Γ. Remarkably, instead of annihilating, we find that the principal nodes "bounce" in the $(1\bar{1})$ direction, where they follow their adjacent counterparts, as visible at $t=0$. Fig. 2**b** shows the full 2D band structure at this very time. At $t=2$, the two adjacent nodes meet at M and also fail to annihilate, as can be seen at time $t=4$ where they progress towards Γ. At $t=8$, the adjacent nodes have been annihilated at Γ. Finally, at $t=10$, the principal nodes have been annihilated at M, and the three bands have become been gapped out again.

Non-Abelian topological obstruction.— The path-dependent capability of band nodes to annihilate, exemplified by the model in Eq. (1), is a consequence of an underlying non-Abelian topology. While non-trivial exchange of band nodes in momentum space has first been reported by Ref. [18] in the context of nodal lines in $\mathcal{PT}$-symmetric systems, we uncover that point nodes are more suitable for experimental studies, while also offering an easier implementation of the braiding. Importantly, we significantly simplify the mathematical description of the non-Abelian topology. After identifying the essence of the nontrivial braid factors by encoding the underlying Hamiltonian using orthonormal frames [18], we express the capability of nodes to pairwise annihilate using the appropriate geometric concepts [19, 20].

For a two-dimensional system, we note [17] that $C_2\mathcal{T}$ symmetry implies the existence of a basis in which the Bloch Hamiltonian $\mathcal{H}(\boldsymbol{k})$ is a real symmetric matrix. The model in Eq. (1) can be brought to such real form by a unitary rotation, $H(\boldsymbol{k}) \to V \cdot H(\boldsymbol{k}) \cdot V^\dagger$, where $V = \sqrt{1 \oplus \sigma_x}$ [the square root of the permutation matrix $(123) \leftrightarrow (132)$]. As a consequence, the Bloch states can be identified as *purely real* vectors. If we further focus on momenta $\boldsymbol{k}$ where the energy bands are non-degenerate, then we can form an energetically ordered set of the N Bloch states, $\{|u^j(\boldsymbol{k})\rangle\}_{j=1}^N =: F(\boldsymbol{k})$. The orthogonality and the reality of the vectors allow us to interpret this collection as an orthonormal *frame* [18], Crucially, we can assign a *frame-rotation charge* to each closed path that avoids band nodes [17]. If one varies the momentum along a closed path based at $\boldsymbol{k}$, the Hamiltonian returns to its original form. Nonetheless, the initial and the final frame at $\boldsymbol{k}$ may differ in the relative orientation of some of the vectors, thereby altering the triad that spans the frame. Notably, such a transformation occurs if one encircles a band node. As one moves along a tight loop around the node formed by a pair of bands, then the two vectors describing those bands perform a π-rotation, while the other bands are essentially constant. This corresponds to an overall π rotation of the frame F, and results in a π Berry phase carried by the node [21–23].

Given two nodes inside the same band gap, one may wonder how their associated frame rotations compose to-

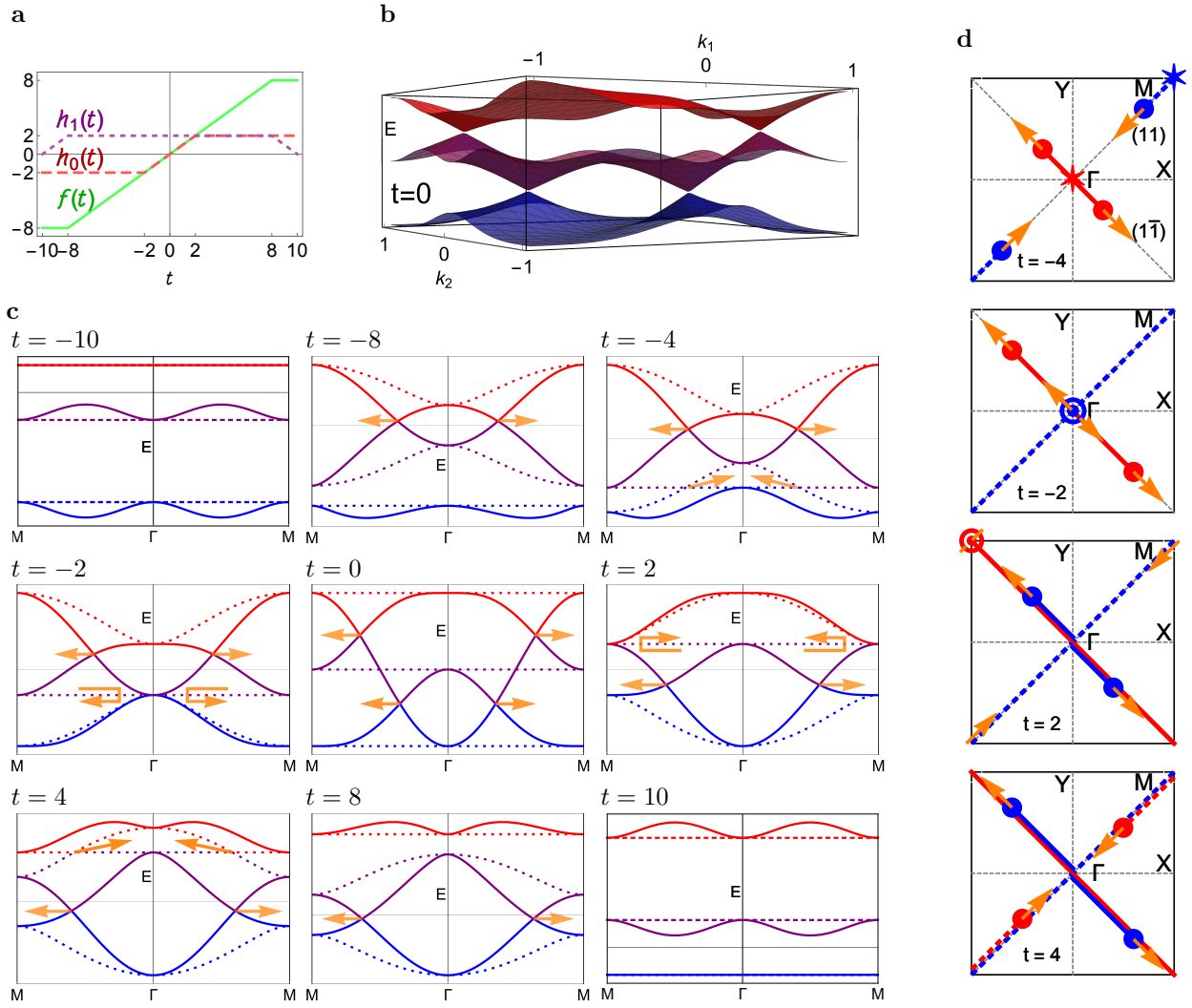

FIG. 2. **Braiding protocol. a.** Control parameters during the braiding protocol. **b.** 2D band structure at $t = 0$ where both principal and adjacent nodes coexist along the diagonal $(1\bar{1})$. **c.** Band structures along the two diagonals of the Brillouin zone, i.e. $(1\bar{1})$ (full lines) and (11) (dashed), at successive instants of the adiabatic parameter $t \in [-10, 10]$. **d.** Schematic configuration of the nodal points over the 2D Brillouin zone with their past trajectory at a few instants (the dashing matches with **c.**). At $t = -2$, the principal nodes meet exactly at Γ but fail to annihilate. At $t = 2$, the adjacent nodes meet exactly at M without annihilating each other. The orange arrows represent the motion of the nodal points.

gether. One possibility is that the second rotation undoes the first, e.g. if we rotate by π in the reverse direction. In that case the two nodes annihilate when brought together. Alternatively, the rotations could revolve in the same direction. Although the total 2π rotation looks like a do-nothing transformation, simple manifestations such as the Dirac's belt trick [24] reveal that a 2π rotation cannot be trivially undone (while a 4π rotation can). Mathematically, this corresponds to the non-trivial fundamental group $\pi_1[\mathrm{SO}(N)] = \mathbb{Z}_2$, for $N > 2$. Physically, this implies that a pair of nodes associated with a 2π frame rotation cannot annihilate [20].

For the three-band model in Eq. (1), we study in Fig. 3 the accumulated frame-rotation angle on two paths that enclose the two principal nodes. More precisely, we decompose the 3D rotation matrix using the generators $L_{x,y,z}$ as $R = \exp[\alpha L_x + \beta L_y + \gamma L_z]$, and define the rotation angle as $\varphi = \sqrt{\alpha^2 + \beta^2 + \gamma^2}$. As anticipated, we find that the accumulated rotation angle equals 0 (2π) if the nodes can (cannot) annihilate. The difference for the two paths originates from the noncommutativity of rotations. More specifically, the rotation angle α acquired as one traverses around the principal node is *reversed* after conjugation with the overall $\pm\pi$ rotation associated with the adjacent node ($\mathrm{e}^{\pi L_j}\mathrm{e}^{\alpha L_i}\mathrm{e}^{\pi L_j} = \mathrm{e}^{-\alpha L_i}$ for $i \neq j$) [17]. As a consequence, the topological charge of principal nodes *anticommutes* with the topological charge of the adjacent nodes. This property can be modelled by the quaternion group $\mathsf{Q} = \{\pm 1, \pm \mathrm{i}, \pm \mathrm{j}, \pm \mathrm{k}\}$, as illustrated in Fig. 1**b**.

Mathematically speaking, the orthonormal frame $F(\boldsymbol{k})$ has a gauge degree of freedom, preserving the reality con-

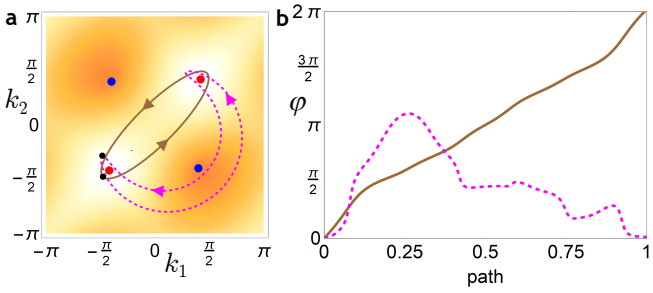

FIG. 3. **Frame-rotation charge. a.** The red (blue) points indicate the principal (adjacent) nodes of the model in Eq. (1) for $t = -4$. The shades of orange on the background indicate the magntitude of the principal gap, with white denoting the band nodes and higher color intensity signaling a larger gap. The oriented solid brown and dashed purple lines indicate two trajectories to enclose the principal nodes, with initial points marked with black dots. **b.-c.** The total frame-rotation angle along the two trajectories displayed in panel **a.**.

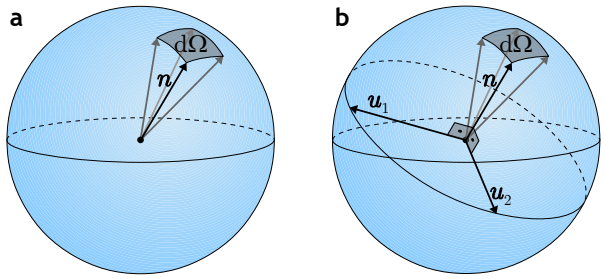

FIG. 4. **Berry curvature vs. Euler form. a.** For two-band Hamiltonians, the integral of Berry curvature over a patch $\mathrm{d}k_x\mathrm{d}k_y$ corresponds to one half of the solid angle $\mathrm{d}\Omega$ spanned by a unit vector $\boldsymbol{n}$ as momentum is varied over the patch. The vector $\boldsymbol{n}$ represents a parameterization of the Hamiltonian in terms of Pauli matrices, as explained around Eq. (3). **b.** Similarly, for three-band Hamiltonians with $C_2\mathcal{T}$ symmetry, an analogous integral of Euler form over two bands $\{|u_1\rangle, |u_2\rangle\}$ corresponds to the solid angle spanned by the unit vector $\boldsymbol{n} = \boldsymbol{u}_1 \times \boldsymbol{u}_2$.

dition, which corresponds to inverting the overall sign of any of the vectors. This exactly coincides with a gauge description of the order parameter space of a biaxial nematic [25], $M = \mathsf{SO}(3)/D_2$, where D_2 is the dihedral crystallographic point group [18]. Consequently, closed paths in M are described by the fundamental group $\pi_1[M]$, being the quaternion group [26–32]. Heuristically, the transformation corresponds to creating disclinations that arise upon performing π-rotations around each of the three axes, the processes of which can be described by the Pauli matrices, illuminating the appearance of quaternionic charges from afifferent point of view.

Although the calculation of the total frame-rotation angle successfully indicates the capability of band nodes to pairwise annihilate, such algorithm has two major deficiencies. First, the commutation relation for rotation matrices is difficult to visualize. Second, and more severely, such approach becomes computationally inefficient for models with many bands, such as obtained in first-principles calculations. To overcome both issues, we present in the next section an alternative algorithm for the band node diagnosis.

Euler form.— The capability of nodes to annihilate can be efficiently formulated using *Euler form*. Here, we introduce this mathematical object, while the application to the model in Eq. (1) is presented in the next section. If $\left|u^1(\boldsymbol{k})\right\rangle$ and $\left|u^2(\boldsymbol{k})\right\rangle$ denote the Bloch states of the two principal bands, then their Euler form is [33]

$$\mathrm{Eu}(\boldsymbol{k}) = \left\langle \boldsymbol{\nabla} u^1(\boldsymbol{k}) \right| \times \left| \boldsymbol{\nabla} u^2(\boldsymbol{k}) \right\rangle . \tag{2}$$

Although Euler form can be formulated more generally for any even number of bands [34], the two-band formulation is sufficient for the problem of band-node braiding [17]. The integral of Euler form over a closed surface gives an integer topological invariant called *Euler class* [35], analogous to the way Berry curvature on a closed surface integrates to an integer invariant called (first) Chern number. Euler form and Euler classe can be understood as refinements of Berry curvature and of Chern number for real symmetric Hamiltonians [36].

We motivate the quantization of Euler class by drawing an analogy to Chern number for a two-band model $\mathcal{H}(\boldsymbol{k}) = \boldsymbol{h}(\boldsymbol{k}) \cdot \boldsymbol{\sigma}$, where $\{\sigma_i\}_{i=1}^3$ are the Pauli matrices and $\boldsymbol{h}(\boldsymbol{k})$ is a three-component real vector. The integral of Berry curvature over an infinitesimal domain $\mathrm{d}k_x\mathrm{d}k_y$ can be expressed [2] as one half of the solid angle

$$\mathrm{d}\Omega = \boldsymbol{n} \cdot \left(\partial_{k_x}\boldsymbol{n} \times \partial_{k_y}\boldsymbol{n}\right) \mathrm{d}k_x\mathrm{d}k_y \tag{3}$$

that is covered by the unit vector $\boldsymbol{n}(\boldsymbol{k}) = \boldsymbol{h}(\boldsymbol{k})/\|\boldsymbol{h}(\boldsymbol{k})\|$ as $\boldsymbol{k}$ ranges over the domain, as shown in Fig. 4**a**. If momentum ranges over a *closed* manifold, then $\boldsymbol{n}$ wraps around the unit sphere (i.e. the manifold of unit vectors) an integer number of times. This implies that Berry curvature integrates to integer multiples of 2π. The integer coefficient is called the Chern number. In models with additional bands, the construction using the unit sphere becomes inadequate, but the quantization still follows from the theory of characteristic classes [37].

In analogy, the simplest scenario with a non-trivial Euler class over two principal bands occurs in three-band models. We find [17], as illustrated in Fig. 4**b**, that the integral of the Euler form over an infinitesimal domain $\mathrm{d}k_x\mathrm{d}k_y$ is equal to the solid angle $\mathrm{d}\Omega$ in Eq. (3) (without the 1/2 factor), where now $\boldsymbol{n} = \boldsymbol{u}_1 \times \boldsymbol{u}_2$ is the cross product of the real three-component vectors representing the principal bands. Using analogous arguments as before, one concludes that for three-band models the Euler form on closed manifolds integrates to integer multiples of 4π. While the simple geometric interpretation of the Euler form becomes insufficient in models with additional bands, it follows from the theory of characteristic classes [17, 37] that quantization to integer multiples of 2π persists, and

$$\chi = \frac{1}{2\pi} \oint \mathrm{Eu}(\boldsymbol{k})\, \mathrm{d}k_x\mathrm{d}k_y \tag{4}$$

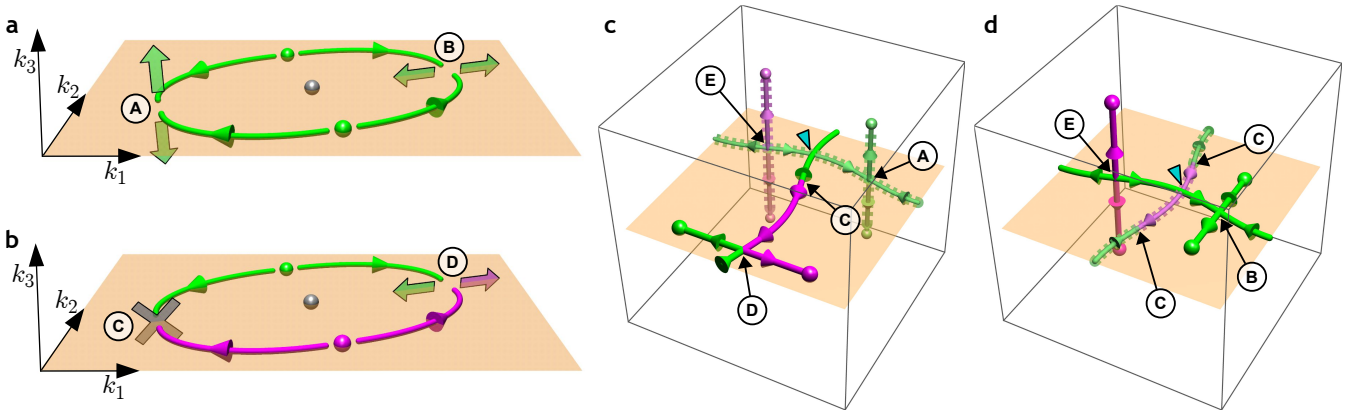

FIG. 5. **Braiding of Weyl points (WPs) in 3D momentum space. a.** Two principal WPs (spheres) with *equal* chirality (green color) which are pinned to plane $k_z = 0$ (orange sheet) can be brought together on two sides of an adjacent WP (grey sphere). After the collision, the two principal WPs can either symmetrically leave the plane (**A**), or remain pinned inside the plane (**B**), depending on their total frame-rotation charge. **b.** Analogous situation involving two principal WPs with *opposite* chirality (green vs. magenta color). After the collision, two such WPs can either annihilate (**C**) or remain pinned inside the plane (**D**), depending on their total frame-rotation charge. The processes (**A–D**) can also be realized in the reverse direction, and can be also exhibited by adjacent nodes. **c.–d.** Motion of WPs inside the 3D Brillouin zone for tight-binding models presented in the Supplemental Material [17]. Solid opaque (ragged transparent) lines indicate trajectories of principal (adjacent) WPs, and the magenta (green) color indicates WPs with positive (negative) chirality. Spheres indicate the position of the WPs at the end of the protocol. Besides processes (**A–D**), both protocols also exhibit a simultaneous creation of two in-plane WPs of one chirality with two out-of-plane WPs of the other chirality (**E**). Intersection of trajectories indicated with cyan triangles do not correspond to WP collisions. Rather, they imply exchange (i.e. braiding) of principal and adjacent WPs, which explains the altered behavior of the two principal WPs between their pairwise creation and their pairwise bounce.

is an integer number called the Euler class. For reasons discussed in the Supplemental Material [17], the Euler form is well defined only in the absence of adjacent nodes. On the other hand, although principal nodes produce discontinuities of the Euler form, the form remains bounded and integrable [17].

Band node diagnosis from Euler class.— To predict whether a pair of principal nodes annihilate when brought together along a specified trajectory, we find a region (disk) $\mathcal{D}$ that (i) contains the trajectory, and that (ii) does not contain any additional principal nor adjacent nodes. For regions with a boundary, the integral of the Euler form ceases to be quantized. This is analogous to the fact that Berry curvature on manifolds with a boundary does not integrate to an integer Chern number. In both cases, the quantization is restored by combining the surface integral with a contour integral of a connection over the boundary.

Euler form exhibits discontinuities at the principal nodes, which prevents the two integrals from cancelling each other [17]. Assuming that $\mathcal{D}$ contains an *even* number of principal nodes, one can find a continuous real gauge for the principal bands over the whole boundary $\partial\mathcal{D}$, which implies a unique value of the Euler connection $\mathbf{a}(\boldsymbol{k}) = \langle u^1(\boldsymbol{k})|\boldsymbol{\nabla} u^2(\boldsymbol{k})\rangle$ on the boundary. We find [17] that the Euler class over $\mathcal{D}$,

$$\chi(\mathcal{D}) = \frac{1}{2\pi}\left[\int_{\mathcal{D}} \mathrm{Eu}(\boldsymbol{k})\,\mathrm{d}^2k - \oint_{\partial\mathcal{D}} \mathbf{a}(\boldsymbol{k})\cdot\mathrm{d}\boldsymbol{k}\right], \quad (5)$$

is an integer topological invariant. If the principal nodes inside $\mathcal{D}$ are able to annihilate, this integer must be zero. This follows because annihilating all the nodes inside the disc makes the Euler form continuous inside the disc, in which case the Stokes theorem leads to cancellation of the two integrals. In contrast, a non-zero value of $\chi(\mathcal{D})$ indicates an obstruction for annihilating the principal nodes. We confirm such a correspondence for the model in Eq. (1) using numerical studies presented in the Supplemental Material [17]

Non-Abelian conversions in $(3+1)D$.— Having obtained an understanding of the non-Abelian topological charge of point nodes in two dimensions, we move our attention to systems with three spatial dimensions. It is well understood [38] that $C_2\mathcal{T}$ symmetry can stabilize Weyl points (WPs) *inside* high-symmetry planes, as observed in the $k_z = 0$ plane of WTe_2 [39], $MoTe_2$ [40] and LaAlGe [41]. While such WPs are characterized by their chiral charge [11], the $C_2\mathcal{T}$ symmetry assigns them an extra frame-rotation charge defined by the Hamiltonian inside the symmetric plane. Importantly, these charges carry complementary pieces of topological information. While the chiral charge discloses whether a pair of WPs can annihilate, the frame-rotation charge conveys whether the two WPs can disappear from the symmetric plane.

Four scenarios are possible, as illustrated in Fig. 5**a**–**b**, which show the braiding of principal WPs (marked in green vs. magenta distinguishing their chirality) around an adjacent node (marked in gray). Starting with two WPs of equal chirality within the symmetric plane, they can either leave the plane (**A**) or bounce within the plane

(**B**) when collided. Considering instead two principal WPs of opposite chirality, they can either annihilate each other (**C**) or bounce within the plane (**D**). In cases (**B**) and (**D**), the two principal WPs carry a nontrivial frame-rotation charge that obstructs their disappearance from the symmetric plane, independently of their chirality. In cases (**A**) and (**C**), the frame-rotation charge is trivial, allowing the pair of principal WPs to disappear from the plane.

In Fig. 5**c**–**d** we illustrate the four scenarios using data obtained from explicit 3D tight-binding models, detailed in the Supplemental Material [17]. The trajectories of the principal WPs (solid opaque lines) and adjacent WPs (ragged transparent lines) are marked according to their chirality (green vs. magenta) and are given a time direction through the arrows. The spheres indicate the position of the WPs at the end of the protocol. In both cases we assume that two adjacent WPs are first created within the symmetric plane [(**E**) in Fig. 5**c**, and (**C**) in Fig. 5**d**], which are then driven through a non-contractible loop in the Brillouin zone, each WP in opposite direction, until they disappear by colliding at the end of their trajectories within the plane [(**A**) in Fig. 5**c**, and (**C**) in Fig. 5**d**]. Then follows the creation of two principal WPs within the symmetric plane [(**C**) in Fig. 5**c**, and (**E**) in Fig. 5**d**], that are sent in opposite directions over a non-contractible path in the Brillouin zone that crosses the past trajectory of the adjacent WPs. This induces a non-trivial frame-rotation charge upon the principal WPs at the end of their trajectories, such that these experience an obstruction to leave the plane [(**D**) in Fig. 5**c**, and (**B**) in Fig. 5**d**].

Experimental implementation.— We now turn to the experimental relevance of our framework. Given the concrete nature of our model, a first promising direction entails implementation in the context of cold atom systems. Indeed, a three-site basis can be employed to directly engineer Hamiltonian (1), whereas synthetic dimensions can also be employed to access the three-dimensional model. Moreover, recent experimental studies have reported on techniques to measure geometric Wilson phases [42]. That is, upon detecting changes in band populations under the influence of an external force, elements of the Berry-Wilczek-Zee connection [43] can be obtained. We note that taking a consistent patch in momentum space in this setup exactly matches with taking the right gauge conditions in the above geometrical description. Additionally, generalizations of methods, e.g. focusing on the principle bands, to reconstruct the Berry curvature using tomography, should be possible [44]. Next to cold atom realizations, photonic systems offer a promising venue to implement our scheme. In particular, using the waveguide setup that was recently employed to measure second Chern numbers [45], the model Hamiltonian can be realized on a 2D surface, whereas the extra z-direction acts as an adiabatic time parameter to accomplish the protocol outlined in Figs. 1 and 2. Apart from these direct pursuits, our analysis also opens up material searches to implement the conversion effect. In particular, we anticipate that the recent progress in the analysis of van der Waals heterostructures should entail an interesting research direction. Studies into twisted bilayer graphene [46] have identified the existence of non-trivial bands in terms of the above characterization under $C_2\mathcal{T}$ symmetry [35, 47]. The flexibility of the stacking direction (also under stress, strain and voltage/potential differences for e.g the p_z band [47]) could be utlized to implement the above physics in such systems. We also remark the pioneering experimental efforts to move the WPs of WTe_2 through $\boldsymbol{k}$-space by driving an optical "shear" phonon mode, reported by Ref. [48].

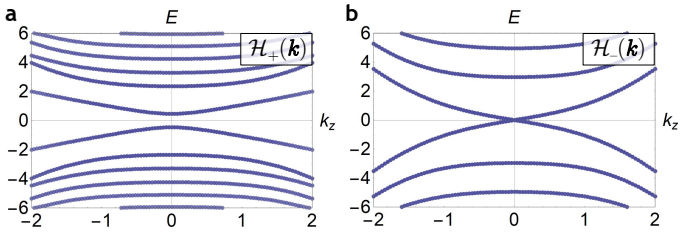

FIG. 6. **Signature of the non-Abelian topology in Landau levels.** Landau levels (LLs) of the Hamiltonian in Eq. (6) (**a**), resp. in Eq. (7) (**b**), for $m = -0.5$. Both models exhibit a pair of Weyl points of opposite chirality at the exact same locations. The chiral Landau levels of the model with trivial (non-trivial) frame-rotation charge are found to hybridize (cross).

Finally, we like to illustrate the existence of a general observable of frame-rotation charge, being distinct behavior in the Landau level spectrum depending on whether the nodes can annihilate or not. Assuming momenta and Hamiltonian parameters sufficiently close to the Weyl collision point, the third band is approximately constant and can be neglected. As a result, the effective physics can be modelled with two-band $\boldsymbol{k}\cdot\boldsymbol{p}$ Hamiltonians. Assuming two WPs of opposite chirality that have a trivial (+) vs. non-trivial (−) total frame-rotation charge, we obtain [17]

$$\mathcal{H}_+(\boldsymbol{k}) = 2(k_xk_y+m)\sigma_x + \quad k_z\sigma_y + (k_x-k_y-k_z^2)\sigma_z \quad (6)$$
$$\mathcal{H}_-(\boldsymbol{k}) = 2(k_xk_y+m)\sigma_x + k_xk_z\sigma_y + (k_x^2-k_y^2-k_z^2)\sigma_z \quad (7)$$

Both models exhibit a pair of WPs at the identical locations for $m<0$. However, while the WPs of $\mathcal{H}_+(\boldsymbol{k})$ annihilate at $m=0$, the non-trivial winding [38] of the frame describing $\mathcal{H}_-(\boldsymbol{k})$ forces the corresponding two WPs to bounce inside the plane. We find [17] that the chiral Landau levels of $\mathcal{H}_+(\boldsymbol{k})$ hybridize, and open an energy gap, while the chiral Landau levels of $\mathcal{H}_-(\boldsymbol{k})$ cross, cf. Fig. 6. The latter case resembles the Landau levels of a massless Dirac Hamiltonian and hence we expect negative longitudinal mangetoresistance (and other signatures of the chiral anomaly) in such perpendicular fields only when the frame-rotation charge prevents the Weyl points from annihilating.

Conclusions.— In this paper we presented experimentally relevant models and protocols to uncover a novel

non-Abelian braiding effect for momentum space band nodes of $C_2\mathcal{T}$-symmetric systems. In addition, we have presented a mathematically rigorous but physically appealing analysis to characterize these phenomena by introducing the notion of Euler form. The observation of the discussed effects is within the reach of current experimental techniques, and we are therefore hopeful that our study will prove impactful in the near future. This is also reflected in a number of follow-up pursuits, such as extending the mathematical structure to reveal novel types of charges and exploring other physical signatures, e.g on the edge, as well as *ab initio* searches.

Acknowledgments

Acknowledgements.— We acknowledge valuable discussions with C. C. Wojcik and A. Vishwanath. R.-J. S acknowledges funding via A. Vishwanath from the Center for the Advancement of Topological Materials initiative, an Energy Frontier Research Center funded by the U.S. Department of Energy, Office of Science. T. B. was supported by the Gordon and Berry Moore Foundation's EPiQS Initiative, Grant GBMF4302.

Authors Contributions

All authors contributed equally to all the main aspects of the work. A. B. developed the tight-binding models detailed in the Supplemental Material. R.-J. S. considered the relation to experiment. T. B. typed Secs. **B** to **J** of the Supplemental Material.

List of contents

This document contains supplemental information, which has been omitted from the main text to keep it brief and simple. We have organized the information into sections, as follows:

A. Tight-binding models and numerical results

A1. Generic tight-binding model

We derive a generic three-dimensional three band tight-binding model with the single constraint that it satisfies $C_2\mathcal{T}$ symmetry with $(C_2\mathcal{T})^2 = +1$, and given a choice of the Wyckoff positions. $C_2\mathcal{T}$ symmetry requires the magnetic space group $P12'1$ (#3.3.10) as minimal subgroup [49, 50], i.e. the direct product between the primitive monoclinic Bravais lattice as the normal subgroup of translations and the magnetic point group $2' = \{E, C_2\mathcal{T}\}$ (#3.3.8) with $\hat{y}$ as the C_2 rotation axis [49, 50].

We choose the primitive lattice vectors as $\boldsymbol{a}_1 = a(\sin\theta, 0, \cos\theta)$, $\boldsymbol{a}_2 = b(1,0,0)$, and $\boldsymbol{a}_3 = c(0,1,0)$, and write their dual (primitive reciprocal lattice vectors) as $\{\boldsymbol{b}_1, \boldsymbol{b}_2, \boldsymbol{b}_3\}$ ($\boldsymbol{a}_i \cdot \boldsymbol{b}_j = 2\pi\delta_{ij}$) taken as the basis for the Bloch wave vector (momentum) $\boldsymbol{k} = (k_1\boldsymbol{b}_1 + k_2\boldsymbol{b}_2 + k_3\boldsymbol{b}_3)/2$. Note that the C_2 rotation axis ($\hat{y}$ as in [49]) is $\boldsymbol{a}_3$ in our basis, i.e. it acts component-wise on the momentum as $C_2(k_1, k_2, k_3) = (-k_1, -k_2, k_3)$. The C_2 rotation axis then defines a basal plane perpendicular to it.

We note that the advantage of the crystallographic convention (C_2 taken along $\hat{y}$) is that if we choose $\hat{z}$ as the quantization axis for the spin, the representation of $C_2^{(\hat{y})}\mathcal{T}$ symmetry on the pure spinor basis $(\phi_\uparrow, \phi_\downarrow)$ takes the simple form $(-i\sigma_y)(i\sigma_y\mathcal{K}) = \mathbf{1}\mathcal{K}$ (where $\mathcal{K}$ is complex conjugation), i.e. it makes explicit the fact that it acts trivially on the spin degrees of freedom. As a consequence our model below holds both for spinfull and spinless systems, since it is constrained only by $C_2\mathcal{T}$ symmetry. Form now on we thus discard spin indices and remark when a statement is only valid for the spinless case.

In the following we make the assumption that one real s-wave orbital sits on Wyckoff's positions $1b$ and $2e$ [49]. Since $2e$ is twofold ($1b$ is invariant under C_2, $2e$ is not) there are three sub-lattice sites per unit cell. We take their locations within the n-th unit cell as $\{\boldsymbol{R}_n + \boldsymbol{r}_\alpha\}_{\alpha=A,B,C}$, with $\boldsymbol{r}_A = (0,0,0)$ for $1b$, and $\boldsymbol{r}_B = (u,v,w)$ and $\boldsymbol{r}_C = (-u,-v,w)$ for $2e$ (here and in the following we write all vectors of the direct space in the primitive basis $\{\boldsymbol{a}_i\}_{i=1,2,3}$). We write the localized Wannier function for the α-th orbital of the n-th unit cell as $|w, \boldsymbol{R}_n + \boldsymbol{r}_\alpha\rangle$. The Bloch basis is then given through the discrete Fourier transform as

$$|\varphi_\alpha, \boldsymbol{k}\rangle = \frac{1}{\sqrt{N_\alpha}} \sum_{\boldsymbol{R}_n} e^{i\boldsymbol{k}\cdot\boldsymbol{R}_n} |w, \boldsymbol{R}_n + \boldsymbol{r}_\alpha\rangle\,,\ \alpha = A, B, C\,, \tag{1}$$

with N_α the number of lattice sites with an α-orbital. In the following we use the vector notation $|\boldsymbol{\varphi}, \boldsymbol{k}\rangle = (|\varphi_A, \boldsymbol{k}\rangle, |\varphi_B, \boldsymbol{k}\rangle, |\varphi_C, \boldsymbol{k}\rangle)^T$. $C_2\mathcal{T}$ symmetry acts then as

$$^{C_2\mathcal{T}}|\boldsymbol{\varphi}, \boldsymbol{k}\rangle = |\boldsymbol{\varphi}, (k_1, k_2, -k_3)\rangle(1 \oplus \sigma_x)\mathcal{K}\,. \tag{2}$$

We can now write the Bloch tight-binding model

$$\mathcal{H} = \sum_{\boldsymbol{k}\in \mathrm{BZ}} |\boldsymbol{\varphi}, \boldsymbol{k}\rangle H(\boldsymbol{k}) \langle\boldsymbol{\varphi}, \boldsymbol{k}|\,, \tag{3}$$

with the matrix components

$$H_{\alpha\beta}(\boldsymbol{k}) = \sum_{\boldsymbol{n}\in\mathbb{N}^3} T_{\alpha\beta}(\boldsymbol{n}) e^{i\boldsymbol{k}\cdot(n_1\boldsymbol{a}_1 + n_2\boldsymbol{a}_2 + n_3\boldsymbol{a}_3)}\,, \tag{4}$$

where the Bloch wave vector $\boldsymbol{k} = (k_1\boldsymbol{b}_1 + k_2\boldsymbol{b}_2 + k_3\boldsymbol{b}_3)/2$ is taken within the first Brillouin zone (BZ), i.e. $(k_1, k_2, k_3) \in (-1, 1]^3$. In the following we also use the rescaled components $\tilde{\boldsymbol{k}} = (\tilde{k}_1, \tilde{k}_2, \tilde{k}_3) \in (-\pi, \pi]^3$.

The hopping parameters $T_{\alpha\beta}(\boldsymbol{n}) \in \mathbb{C}$ are constrained by symmetry. First of all, hermiticity imposes

$$T_{\beta\alpha}(\boldsymbol{n}) = T_{\alpha\beta}(-\boldsymbol{n})^*\,. \tag{5}$$

Then, $C_2\mathcal{T}$ requires

$$(1 \oplus \sigma_x) H^*(k_1, k_2, k_3)(1 \oplus \sigma_x) = H(k_1, k_2, -k_3)\,, \tag{6}$$

which can be recast into the constraints

$$\begin{aligned} &T_{AA}(C_2\boldsymbol{n}) = T_{AA}(\boldsymbol{n})^*\,,\ T_{AC}(C_2\boldsymbol{n}) = T_{AB}(\boldsymbol{n})^*\,,\\ &T_{CC}(C_2\boldsymbol{n}) = T_{BB}(\boldsymbol{n})^*\,,\ T_{CB}(C_2\boldsymbol{n}) = T_{BC}(\boldsymbol{n})^*\,. \end{aligned} \tag{7}$$

In the following we choose the parameters $\{T_{BA}(\boldsymbol{n}), T_{BC}(\boldsymbol{n}), T_{CA}(\boldsymbol{n}), T_{AC}(\boldsymbol{n}), T_{CC}(\boldsymbol{n})\}$ as functions of the other parameters according to Eq. (5) and (7).

A2. Explicit 3D model

Taking the origin $\mathbf{0}$ of the Bravais lattice as a reference and using $\boldsymbol{n}$ of Eq. (4) to label its neighbors, we limit the tight-binding model to the following neighbors: from the basal plane $\boldsymbol{n}_0 \in \{(n_1, n_2, 0) \in \mathbb{N}^2 | n_1, n_2 = -1, 0, 1\}$, from the first plane above $\boldsymbol{n}_u \in \{(n_1, n_2, 1) \in \mathbb{N}^2 | n_1, n_2 = -1, 0, 1\}$, and the first plane below $\boldsymbol{n}_d \in \{(n_1, n_2, -1) \in \mathbb{N}^2 | n_1, n_2 = -1, 0, 1\}$. In the following we use '0', 'u', and 'd' to refer respectively to the basal plane, the upper plane (up), and the lower plane (down).

Let us label the neighbors around within each plane clockwise from 1 to 8 as a function of (n_1, n_2), i.e. $1 : (1,0)$, $2 : (1,1)$, $3 : (0,1)$, $4 : (-1,1)$, $5 : (-1,0)$, $6 : (-1,-1)$, $7 : (0,-1)$, $8 : (1,-1)$, and $0 : (0,0)$, see Fig. S-1. We then use a more compact labeling of the parameters as $\{T_{AA}(\boldsymbol{n}_0)\}_{\boldsymbol{n}_0} = \{a_j^0\}_{j=0,\dots,8}$, $\{T_{AA}(\boldsymbol{n}_u)\}_{\boldsymbol{n}_u} = \{a_j^u\}_{j=0,\dots,8}$, and $\{T_{AA}(\boldsymbol{n}_d)\}_{\boldsymbol{n}_d} = \{a_j^d\}_{j=0,\dots,8}$. We proceed similarly for $T_{BB} = b$, $T_{CC} = c$, $T_{AB} = d$, $T_{AC} = e$, and $T_{BC} = f$, while the labeling of T_{BA}, T_{BC}, and T_{CA} is readily given by hermiticity Eq. (5).

We can now rewrite the constraints following from Eq. (5) and (7) in terms of the compact labeling, i.e.

$$c_{j+4}^\mu = (b_j^\mu)^*,\ c_j^\mu = (b_{j+4}^\mu)^*,\ e_{j+4}^\mu = (d_j^\mu)^*,\ e_j^\mu = (d_{j+4}^\mu)^*,$$

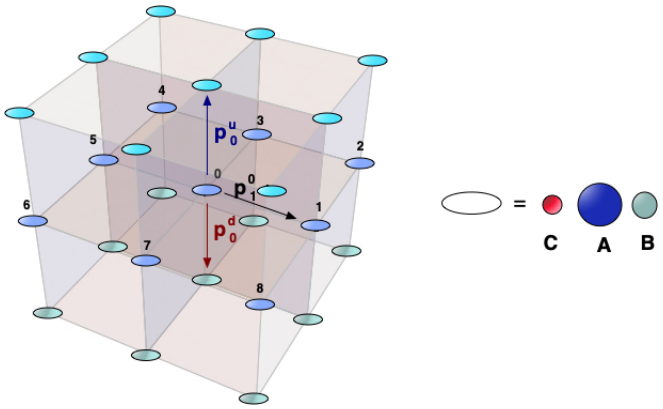

FIG. S-1. Schematic representation of the hopping amplitudes. The 3D model is composed of a three atom basis that is arranged in a simple cubic lattice. Considering the site marked by "0", in-plane hopping is denoted by p_j^0, where j refers to the eight neighbors $1-8$. Similarly, p_j^d and p_j^u denote hopping to a layer beneath and above, respectively. The specific arrangement of these parameters is outlined in the text. The basis units are colored differently depending on the layer to further elucidate the crystal structure.

for $j=1,\dots,4$ and $\mu=0,u,d$, and $c_0^\mu=(b_0^\mu)^*$. Note that since the c's and e's are here all determined by the b's and the d's, respectively, we do not refer to them anymore. Then,

$$a_j^d=a_j^u\ ,\ f_j^d=f_j^u\ ,$$

for $j=0,\dots,8$, and with $a_0^u\in\mathbb{R}$. Furthermore,

$$a_{j+4}^0=(a_j^0)^*\ ,\ b_{j+4}^0=(b_j^0)^*\ ,$$

for $j=1,\dots,4$, and with $a_0^0,b_0^0\in\mathbb{R}$. Finally,

$$b_{j+4}^d=(b_j^u)^*\ ,\ b_j^d=(b_{j+4}^u)^*\ ,$$

for $j=1,\dots,4$, and $b_0^d=(b_0^u)^*$. In the following, any parameter that is not explicitly constrained to be real is considered as a complex number.

We note that from the form of Eq. (4) the three $p_j^{0,u,d}$-terms for fixed $p\in\{a,b,d,f\}$ and $j\in\{1,\dots,8\}$ all have the same (k_1,k_2)-dependence. On the one hand, the p_j^0-terms have no k_3 dependence. On the other hand, the p_j^u- and p_j^d-terms have the form factors of the p_j^0-terms multiplied respectively by $e^{ik_3\pi}$, and by $e^{-ik_3\pi}$. As a consequence, a generic 3D model has the form

$$\begin{aligned}H_{3D}[\{p_j^{0,u,d}\}_{p,j}](k_1,k_2,k_3)&=H_{2D}[\{p_j^0\}_{p,j}](k_1,k_2,0)\\&+H_{2D}[\{p_j^u\}_{p,j}](k_1,k_2,k_3)\\&+H_{2D}[\{p_j^d\}_{p,j}](k_1,k_2,-k_3)\ ,\end{aligned}\tag{8}$$

where $H_{2D}[\{p_j^0\}_{p,j}](k_1,k_2,0)$ is the tight-binding model limited to the basal plane.

A3. Systematic 3D embedding of 2D models

In the three-dimensional Brillouin zone $k_3=0$ and $k_3=1$ define the two $C_2\mathcal{T}$ symmetric planes. The non-Abelian braiding of Weyl points happens within these planes. For clarity we isolate the braiding protocol to the plane $k_3=0$ by requiring that all the $\boldsymbol{k}$-dependent terms vanish at $k_3=1$ which guarantees that the band structure is featureless there. It is now straightforward from Eq. (8) to define the conditions that realizes this. Indeed, from

$$\begin{aligned}H_{3D}[\{p_j^{0,u,d}\}_{p,j}](k_1,k_2,1)&=H_{2D}[\{p_j^0\}_{p,j}](k_1,k_2,0)\\&+H_{2D}[\{p_j^u\}_{p,j}](k_1,k_2,1)\\&+H_{2D}[\{p_j^d\}_{p,j}](k_1,k_2,1)\ ,\\&=H_{2D}[\{p_j^0\}_{p,j}](k_1,k_2,0)\\&-H_{2D}[\{p_j^u\}_{p,j}](k_1,k_2,0)\\&-H_{2D}[\{p_j^d\}_{p,j}](k_1,k_2,0)\ ,\end{aligned}$$

we have that $H_{3D}[\{p_j^{0,u,d}\}_{p,j\neq0}](k_1,k_2,1)=0$ is readily satisfied if $p_j^0-p_j^u-p_j^d=0$ for $j\neq0$.

For instance for $p=a$ we get $a_j^0-a_j^u-a_j^d=0$. But since $a_j^d=a_j^u$, it reduces to $a_j^u=a_j^0/2$. For $p=b$ we get $b_j^0-b_j^u-b_j^d=0$. While, in principle, the phases of the $b_j^{0,u,d}$'s free to differ, we take them equal for simplicity without significant loss of generality. Then, by setting $b_j^d=\beta_j b_j^0$, the condition is satisfied for $b_j^u=(1-\beta_j)b_j^0$.

Collecting all the conditions together, these are

$$\begin{aligned}&a_j^u=a_j^0/2\ ,\\&b_j^u=(1-\beta_j)b_j^0\ ,\ \ b_j^d=\beta_j b_j^0\ ,\end{aligned}\tag{9}$$

for $j=1,\dots,4$ and where $\beta_j\in[0,1]$ is a free parameter, and

$$\begin{aligned}&d_j^u=(1-\delta_j)d_j^0\ ,\ \ d_j^d=\delta_j d_j^0/2\ ,\\&f_j^u=f_j^0\ ,\end{aligned}\tag{10}$$

for $j=1,\dots,8$ and where $\delta_j\in[0,1]$ is a free parameter.

As for the $\boldsymbol{k}$-independent terms, we impose the same constraint of cancellation at $k_3=1$ for $a_0^{0,u}$, $b_0^{0,u}$, and $f_0^{0,u}$, while we impose the cancellation condition at $k_3=0$ for $d_0^{0,u,d}$. This allows us to control the gaps between the bands at $k_3=0$ and at $k_3=1$ independently. That gives,

$$\begin{aligned}&a_0^u=a_0^0/2\,,&&b_0^u=b_0^0/2\,,\\&f_0^u=f_0^0/2\,,\\&d_0^u=-(1-\delta_0)d_0^0\,,\ \ &&d_0^d=-\delta_0 d_0^0\ .\end{aligned}\tag{11}$$

Note the minus signs for the $d_0^{0,u,d}$'s.

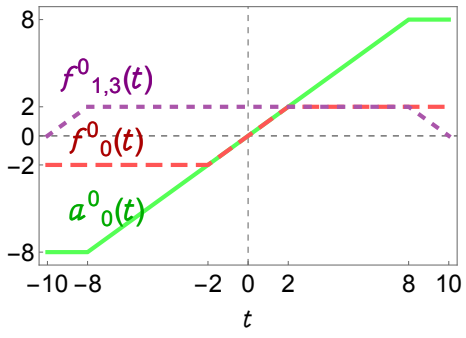

FIG. S-2. Tight-binding parameters of the 2D minimal model as functions of the control parameter t.

A4. Free parameters for the braiding protocol

We list the remaining free parameters from which the protocol of the three-dimensional braiding of Weyl nodes is defined. The free complex variables are $\{a_j^0, b_j^0\}_{j=1,\dots,4}$, $\{d_j^0, f_j^0\}_{j=1,\dots,8}$, and $\{d_0^0, f_0^0\}$. The free real variables are $\{a_0^0, b_0^0\}$, $\{\beta_j\}_{j=1,\dots,4}$, $\{\delta_j\}_{j=1,\dots,8}$, and δ_0.

A5. Minimal 2D model

We define here the 2D minimal model discussed in the main text in terms of the generic tight-binding model introduced above. Since it lies within the basal plane only, we have $p_j^{u,d} = 0$ for all j. Then, among the basal tight-binding terms only the following are set to finite values $\{a_0^0, d_5^0, d_7^0, f_0^0, f_1^0, f_3^0\}$.

Introducing the parameter t that controls the braiding and using the notations of the main text, we obtain the minimal model

$$H_{2D}(\boldsymbol{k};t) = \begin{pmatrix} f(t) & g(\boldsymbol{k}) & g^*(\boldsymbol{k}) \\ g^*(\boldsymbol{k}) & 0 & h(\boldsymbol{k};t) \\ g(\boldsymbol{k}) & h^*(\boldsymbol{k};t) & 0 \end{pmatrix} , \qquad (12)$$

where

$$\begin{aligned} f(t) &= a_0^0(t) \, , \\ g(\boldsymbol{k}) &= d_5^0 \mathrm{e}^{-\mathrm{i}k_1\pi} + d_7^0 \mathrm{e}^{-\mathrm{i}k_2\pi} \, , \\ h(\boldsymbol{k};t) &= f_0^0(t) + f_1^0(t)\mathrm{e}^{\mathrm{i}k_1\pi} + f_3^0(t)\mathrm{e}^{\mathrm{i}k_2\pi} \, , \end{aligned} \qquad (13)$$

and

$$\begin{array}{llll} a_0^0(t) = F_{[8,-]}(t) \, , & f_0^0(t) = F_{[2,-]}(t) \\ d_5^0 = -i \, , & f_1^0(t) = 10 - F_{[8,+]}(t) \, , \\ d_7^0 = i \, , & f_3^0(t) = f_1^0(t) \, , \end{array} \qquad (14)$$

with the t-dependent functions defined through $F_{[\rho,\pm]}(t) = 1/2(|t+\nu| \pm |t-\nu|)$, see Fig. S-2.

As mentioned in the main text, the overly simplified form of the minimal model leads to an effective auxiliary C_2 symmetry

$$U(1 \oplus \sigma_x) H(C_2\boldsymbol{k})(1 \oplus \sigma_x)U^\dagger = H(\boldsymbol{k}) \, , \qquad (15)$$

with $U = \mathrm{diag}(-1,1,1)$ corresponding to the gauge transformation $\phi_A \to -\phi_A$. This can be straightforwardly verified from the explicit expressions Eq. (12) and (13).

As a consequence of this effective symmetry, the band structure is C_2 symmetric and Weyl points (WPs) can only be created four at a time, i.e. two pairs of WPs with opposite chirality. Indeed, any WP at $\boldsymbol{k}$ must have its symmetric partner of equal chirality at $C_2\boldsymbol{k}$, and these must have their symmetric partners of opposite chirality at $-C_2\boldsymbol{k}$ and $-\boldsymbol{k}$ due to $C_2\mathcal{T}$ symmetry.

A6. 3D embedding of the braiding protocol of the minimal 2D model

The minimal 2D model can be readily embedded into 3D by applying the rules of Section A A3. In order to have all bands gaped at $k_3 = 1$, we set the extra parameter $d_0^0 = i4$, while all the other basal parameters are keep the same as in the 2D case. We remark that this preserves the auxiliary C_2 symmetry Eq. (15) so that WPs must be created or annihilated four at a time.

In Fig. S-3 we show the 3D embedding of the minimal 2D model at successive snapshots for $t \in [-10, 10]$. The 3D band structures are represented through two-dimensional slices taken, in one direction, along the diagonals $(1\bar{1}0)$ and (110) (connecting Γ to M), and then (100) (connecting Γ to X), successively, and, in the other direction, along (001), i.e. the C_2 axis perpendicular to the basal plane for $k_3 \in [0,1]$.

We start with the three bands gaped ($t = -10$), then four WPs are created in the second gap at Γ ($t = -9$), with two WPs of equal chirality moving towards M along the $(1\bar{1}0)$ diagonal and two WPs with the other chirality located away from the symmetric plane above and underneath Γ ($t = -8$). Note that by the effective auxiliary C_2 symmetry, the two WPs above and underneath Γ are trapped on the C_2 axis crossing Γ.

At $t = -4$, two WPs of equal chirality have been created in the first gap at M, above and underneath which we find their two partners of creation. The later are again trapped on the C_2 axis crossing M, as imposed by the auxiliary C_2 symmetry. The two WPs within the symmetric plane ($k_3 = 0$) are heading along the diagonal (110) towards Γ, where they meet at the later time $t = -2$. These do not leave the symmetric plane though, as we find them at $t = 0$ moving now along the diagonal $(1\bar{1}0)$.

At $t = 2$, the two WPs of the second gap within the symmetric plane meet at M without leaving the plane, as we can see at $t = 4$ where they now move along (110) towards Γ. At $t = 8$, they have reached Γ where they recombine annihilate with their two partners of creation.

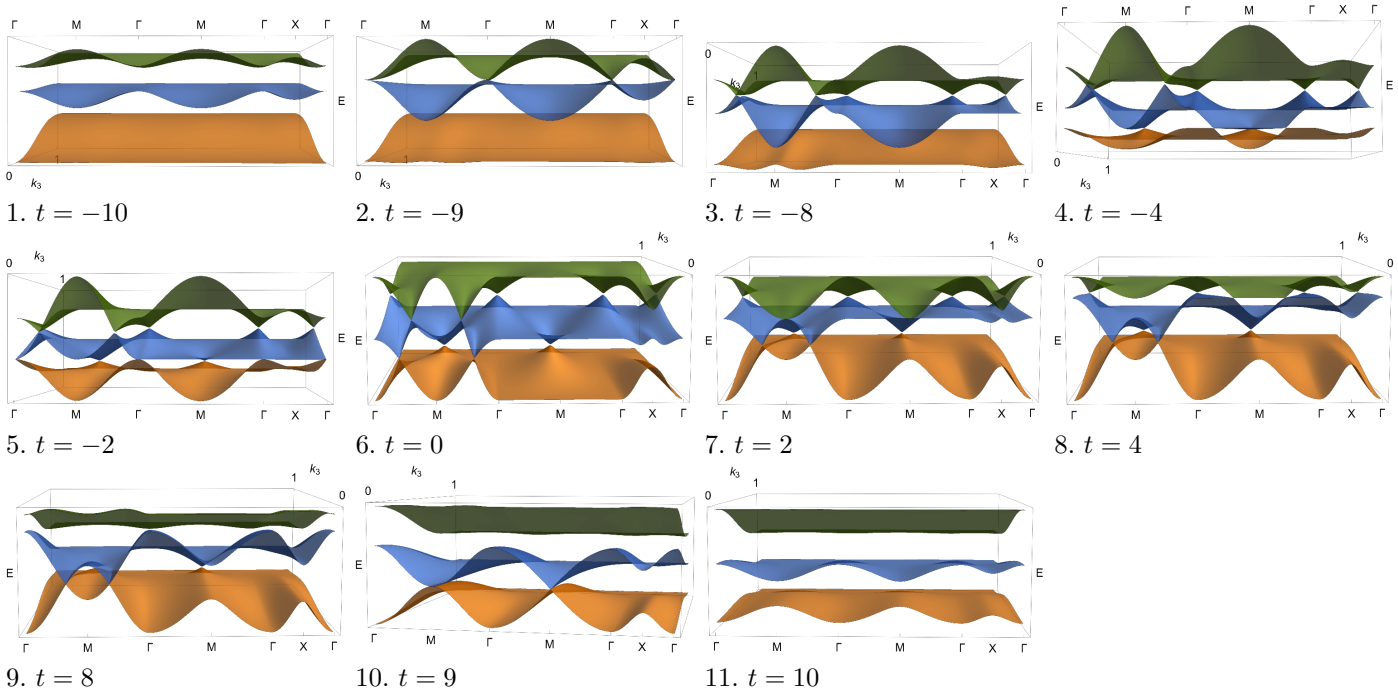

FIG. S-3. **3D embedding of the 2D braiding protocol.** The braiding protocol for the minimal 2D model discussed in the main text is controlled by t. This setup can be embedded in 3D so that the 2D nodal points are realized as Weyl points within a single $C_2\mathcal{T}$ symmetric plane ($k_3 = 0$), and with the three bands gaped on the other symmetric plane ($k_3 = 1$). We draw the two-dimensional slices of the 3D Band structures with the long direction taken as the diagonals $(1\bar{1}0)$ and (110) (connecting Γ to M), and (100) (connecting Γ to X), and with the second direction taken as (001), i.e. for $k_3 \in [0, 1]$ (connecting the two $C_2\mathcal{T}$ symmetric planes).

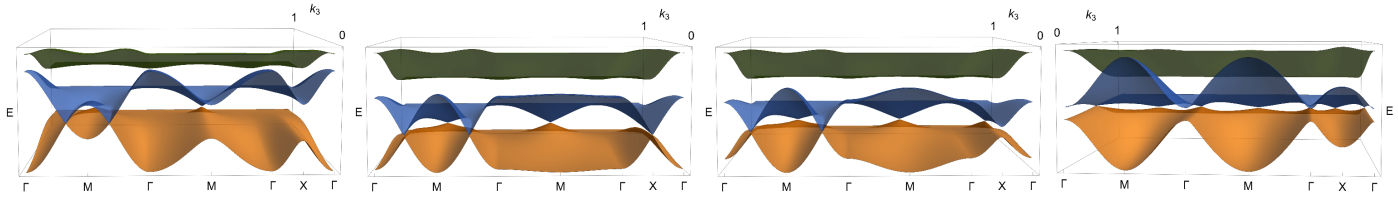

FIG. S-4. **3D embedding without braiding.** When there is no braiding two WPs of equal chirality are allowed to leave the symmetric plane after colliding. The two WPs of the first gap created at M meet at Γ and leave the symmetric plane along the vertical C_2 axis. In the middle of the process, we find that the WPs are converted into a nodal line centered on M that crosses the points X and Y of the Brillouin zone, see panel 2. Then in the tird panel the WPs reappeared on $(1\bar{1}0)$, but four extra WPs have emerged out of the nodal line and populate the two vertical C_2 axes crossing X and Y (here only X is shown). Eventually, the two WPs within the symmetric plane meet at Γ and leave the plane, see final panel.

At $t = 9$, the WPs of the first gap within the symmetric plane meet eventually at M where they also recombine and annihilate with their two partners of creation.

1. *Obstruction versus no obstruction*

As discussed in the main text, the non-Abelian frame-rotation charge captures the stability of two WPs colliding within a $C_2\mathcal{T}$ symmetric plane. We have found above (Fig. S-3) that equal chirality WPs from one gap bounce away as a consequence of the braiding with the WPs of the adjacent gap.

We illustrate now the case without braiding, and hence without obstruction for two WPs of equal chirality to leave the symmetric plane after colliding. This is shown Fig. S-4.

A7. 3D braiding protocol

We present here the numerical data that supports the discussion in the main text of the four scenarios when two principal WPs collide within a $C_2\mathcal{T}$ symmetric plane depending on their braiding with adjacent WPs (see Fig. 5). We organize the braiding protocol such that the obstruction to leave the symmetric plane happens with the principal WPs.

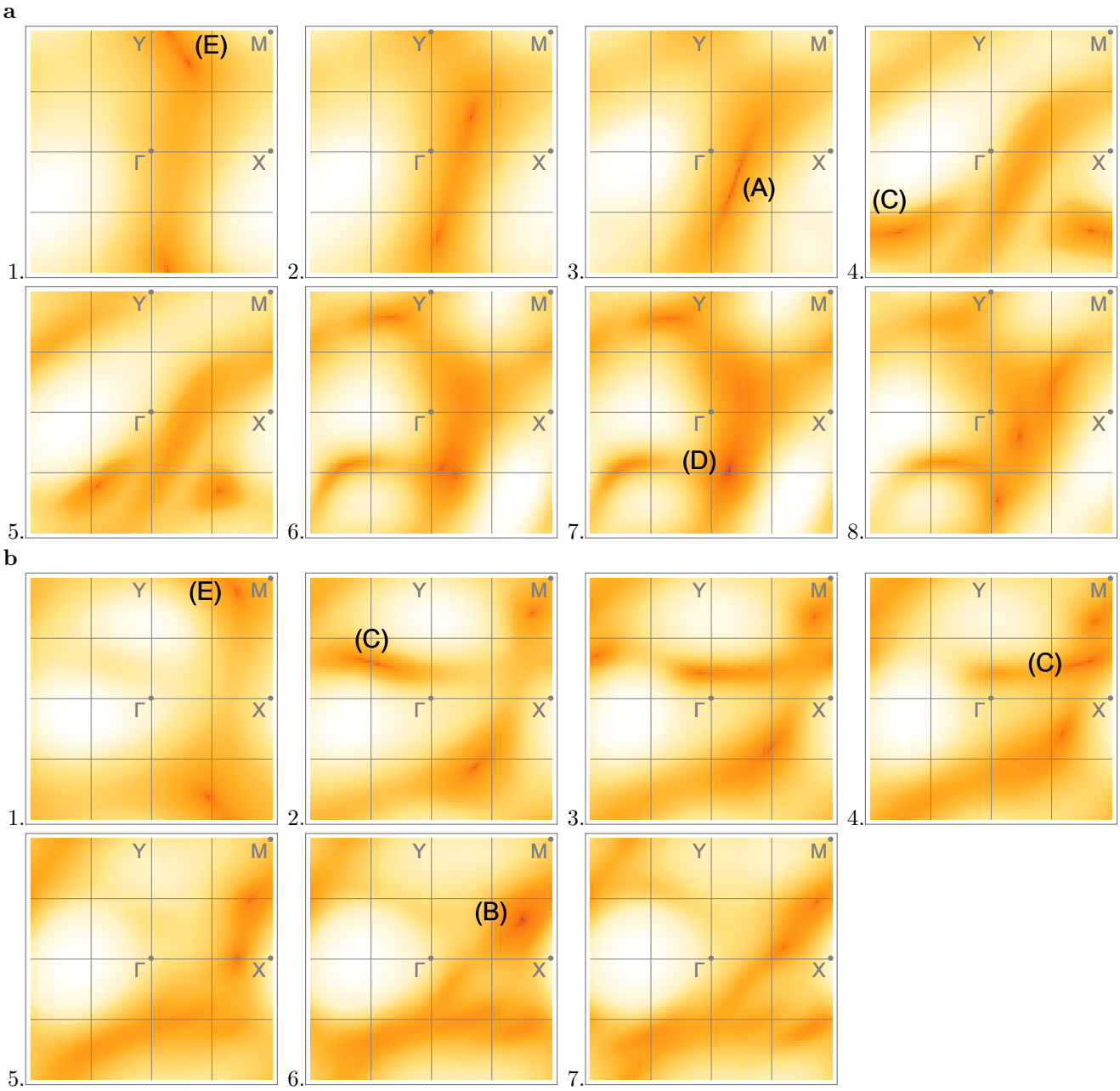

FIG. S-5. **3D braiding protocol.** Product of the magnitude of the two gaps, principal and adjacent, over the 2D Brillouin zone at the symmetric plane $k_3 = 0$. Lighter (darker orange) color indicates larger (smaller) gaps (principal and adjacent combined). The dark spots indicate the location of WPs. **a** Numerical data corresponding to the process of Fig. 5**c** with the successive steps (**E**), and (**A**) for the adjacent WPs, and then (**C**), and (**D**) for the principal WPs. **b** Numerical data corresponding to the process of Fig. 5**d** with the successive steps (**E**) for adj. WPs, (**C**) for princ. WPs, then (**C**) for adjacent WPs, and finally (**B**) for princ. WPs.

In Fig. S-5 we draw the product of the magnitude of the two gaps, principal and adjacent, over the 2D Brillouin zone at the symmetric plane $k_3 = 0$. Lighter (darker orange) color indicates larger (smaller) gaps (principal and adjacent combined). The dark spots indicate the location of WPs.

Fig. S-5**a** (**b**) corresponds to the process of Fig. 5**c** (**d**). Following the main text, we label the processes between two WPs that meet as (**A**), (**B**), (**C**), (**D**), and (**E**), see below and in Fig. 5.

In Fig. S-5**a** we start (panel 1.) with the creation of two secondary WPs of equal chirality within the symmetric plane (**E**). Then we collide them after they run, each in opposite direction, through a non-contractible loop of the Brillouin zone (panels 2. and 3.). Since there has been no braiding for them, they can leave the plane, one above and one below (**A**). A pair of principal WPs of opposite chirality is now created (**C**) (panel 4.). We make them

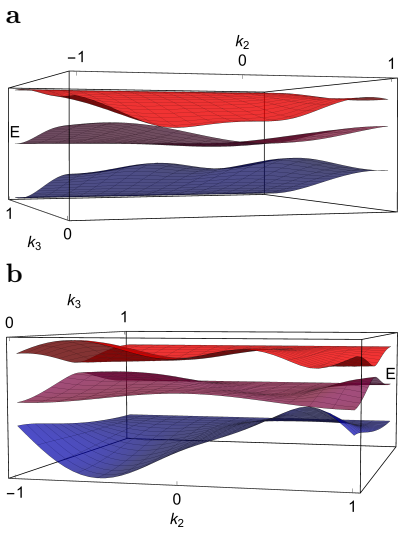

FIG. S-6. **Critical points of the 3D braiding protocol.** **a** Band structure at $k_1 = 0.13\pi$ for $(k_2, k_3) \in [-1, 1] \times [0, 1]$ at the critical point (**D**) of the braiding protocol. **b** Band structure at $k_2 = 0.31\pi$ for $(k_1, k_3) \in [-1, 1] \times [0, 1]$ at the critical point (**B**) of the braiding protocol.

collide after they run, each in opposite direction, along a non-contractible loop that crosses the past trajectory of the adjacent WPs (panels 5., 6., and 7.). Due to the nontrivial frame-rotation charge they acquired through the braiding with the adjacent WPs, these do not annihilate and bounce back within the symmetric plane (**D**) (panel 8.).

In Fig. S-5**b** we start (panel 1.) with the creation of two principal WPs of equal chirality within the symmetric plane (**E**). Two secondary WPs of opposite chirality are then created (**E**), see panel 2. We collide the secondary WPs after they run, each in opposite direction, through a non-contractible loop of the Brillouin zone (panels 3. and 4.). Since there has been no braiding for them, they can leave the plane through annihilation (**C**). We then collide the principal WPs after they run, each in opposite direction, through a non-contractible loop (panels 5. and 6.). Since their trajectory crosses the past trajectory of the adjacent WPs they acquired a nontrivial frame-rotation charge which forbids them from to leave the symmetric plane, so that bounce away within the plane (**B**) (panel 7.).

We show in Fig. S-6**a**, and **b**, the band structures at the critical points when two principal WPs meet exactly before to bounce away through a critical point (**D**), respectively, (**B**). These are two-dimensional slices of 3D band structures with one direction taken within the symmetric plane and the other direction taken along the vertical axis (001) for $k_3 \in [0, 1]$.

B. Reality condition

In the main text, we assumed that $C_2\mathcal{T}$ symmetry automatically implies reality of the Bloch Hamiltonian. While this is not true in general, the conclusions presented in the main text still apply. More precisely, the existence of antiunitary operator $\mathcal{A}$ that obeys (i) $\mathcal{A}^2 = +1$ and (ii) $\forall \boldsymbol{k} : \mathcal{A}\mathcal{H}(\boldsymbol{k})\mathcal{A}^{-1} = \mathcal{H}(\boldsymbol{k})$, implies the existence of a Hilbert-space basis, in which the Hamiltonian $\mathcal{H}(\boldsymbol{k})$ is real. In this section we justify this claim by two different methods. We remark that the antiunitary $\mathcal{A}$ that fulfills the two conditions can be realized as $C_2\mathcal{T}$ in two-dimensional spinful or spinless systems [20], or as $\mathcal{PT}$ in spinless systems of arbitrary dimension [18]. Therefore, for such symmetry settings, both the frame-rotation charge resp. the Euler can be defined if the right Hilbert-space basis has been adopted.

We first prove this statement formally, before providing a physical insight in the next paragraph. Every antiunitary operator $\mathcal{A}$ can be represented as some unitary operator $\mathcal{U}$ composed with the complex conjugation $\mathcal{K}$ [51], i.e. $\mathcal{A} = \mathcal{U}\mathcal{K}$. Unitarity means that $\mathcal{U}\mathcal{U}^\dagger = \mathbb{1}$, while $\mathcal{A}^2 = +\mathbb{1}$ implies that $\mathcal{U}\mathcal{U}^* = \mathbb{1}$. It follows that $\mathcal{U} = \mathcal{U}^\top$. The Autonne-Takagi factorization [52] then guarantees that $\mathcal{U} = \mathcal{V}\mathcal{D}\mathcal{V}^\top$ for some unitary $\mathcal{V}$ and a diagonal matrix $\mathcal{D} = \mathrm{diag}\{e^{i\varphi_j}\}_{j=1}^n$. Constructive and finite algorithms exist that find the Autonne-Takagi decomposition of a symmetric unitary matrix [53]. Rotation of the Hilbert-space by unitary matrix $\sqrt{\mathcal{D}^*}\mathcal{V}^\dagger \equiv \mathcal{W}$ then transform the antiunitary operator to $\mathcal{W}\mathcal{A}\mathcal{W}^\dagger = \mathcal{K}$, i.e. to the form assumed in the main text.

From a physical point of view, it is well known that an antiunitary symmetry squaring to $+1$ (rather than -1) does *not* imply Kramers degeneracies [54]. In other words, eigenstates of $\mathcal{A}$ form generally one-dimensional irreducible representations for this symmetry. By taking these eigenstates to form the basis of the Hilbert space, the antiunitary operator is represented by $\mathcal{D}'\mathcal{K}$, where $\mathcal{D}' = \mathrm{diag}\{e^{i\varphi'_j}\}_{j=1}^n$ is a diagonal matrix of phase factors. Rotating the Hilbert space basis by $\mathcal{W}' = \sqrt{\mathcal{D}'^*}$ then transforms the antiunitary operator to just the complex conjugation $\mathcal{K}$. While the absence of Kramers doubling for such a symmetry is well accepted in the solid-state community, the formal proof of this statement actually follows from the Autonne-Takagi factorization, as discussed in the previous paragraph.

C. Euler form and Euler class

In this section, we outline the mathematical definition of Euler form and of Euler class for real vector bundles. To make the analogy with the Berry curvature and Chern number manifest, we first review the definitions and the properties of these more familiar objects. Note that in this section we adopt the language of differential forms [28], since it allows for more concise expression of

the studied objects and of the relations between them.

We first recall the basic terminology. A collection of n bands over a base space B defines an n-dimensional vector bundle $E \to B$, which is generically *complex*. In this section we assume that the vector bundle is *smooth* (although this assumption would be lifted in later sections, in particular Sec. E). We order the states $\{|u^a(\boldsymbol{k})\rangle\}_{a=1}^n$ as columns into a rectangular matrix $\mathfrak{U}(\boldsymbol{k})$, and we construct the Berry-Wilczek-Zee (BWZ) connection [43]

$$\mathcal{A}(\boldsymbol{k}) = \mathfrak{U}^\dagger(\boldsymbol{k}) d\mathfrak{U}(\boldsymbol{k}), \tag{16}$$

where "d" is the exterior derivative (i.e. the differentiation $d = dk^i \partial_{k_i}$ followed by antisymmetrization in covariant indices [28]). Mathematically, $\mathcal{A}(\boldsymbol{k})$ is a 1-form with values in Lie algebra $\mathfrak{u}(n)$. At the level of individual components, the connection can be expressed as

$$\mathcal{A}_i^{ab}(\boldsymbol{k}) = \left\langle u^a(\boldsymbol{k}) | \partial_{k_i} u^b(\boldsymbol{k}) \right\rangle, \tag{17}$$

where i is a momentum component (the 1-form part), and a, b are band indices (the Lie algebra part). This object is skew-Hermitian in band indices, precisely because $\mathfrak{u}(n)$ constitutes skew-Hermitian matrices. Mixing the n states with a matrix $X(\boldsymbol{k}) \in \mathsf{U}(n)$ as $\tilde{\mathfrak{U}}(\boldsymbol{k}) = \mathfrak{U}(\boldsymbol{k}) X(\boldsymbol{k})$, i.e. performing a *gauge transformation*, transforms the connection as

$$\tilde{\mathcal{A}} = X^{-1} \mathcal{A} X + X^\dagger dX, \tag{18}$$

where we dropped the momentum arguments for brevity.

The BWZ *curvature* is defined as

$$\mathcal{F} = d\mathcal{A} + \mathcal{A} \wedge \mathcal{A}. \tag{19}$$

Mathematically, this is a 2-form with values in $\mathfrak{u}(n)$. Componentwise,

$$\begin{aligned} \mathcal{F}_{ij}^{ab} = &\left\langle \partial_{k_i} u^a | \partial_{k_j} u^b \right\rangle - \left\langle \partial_{k_j} u^a | \partial_{k_i} u^b \right\rangle, \\ &+ \left\langle u^a | \partial_{k_i} u^c \right\rangle \left\langle u^c | \partial_{k_j} u^b \right\rangle - \left\langle u^a | \partial_{k_j} u^c \right\rangle \left\langle u^c | \partial_{k_i} u^b \right\rangle \end{aligned} \tag{20}$$

which is skew-symmetric in momentum coordinates (the 2-form part), and skew-Hermitian in band indices (the Lie algebra part). The curvature transforms covariantly under gauge transformations,

$$\tilde{\mathcal{F}} = X^{-1} \mathcal{F} X \tag{21}$$

which allows us to define a gauge-invariant object, $\mathsf{F} = \mathrm{tr}(\mathcal{F})$, usually called *Berry curvature*. The trace in this definition runs over band indices, i.e. we perform a projection $\mathfrak{u}(n) \to \mathfrak{u}(1)$. Assuming the Einstein summation convention, this amounts to

$$\mathsf{F}_{ij} = \mathcal{F}_{ij}^{aa} = \left\langle \partial_{k_i} u^a | \partial_{k_j} u^a \right\rangle - \left\langle \partial_{k_j} u^a | \partial_{k_i} u^a \right\rangle \tag{22}$$

where the two terms in the second line of Eq. (20) have cancelled each other. One can similarly define *Berry connection* $A = \mathrm{tr}\,\mathcal{A}$. Since the expression $[\mathcal{A} \wedge \mathcal{A}]_{ij} = A_i A_j - A_j A_i$ in Eq. (19) has zero trace, it follows that $\mathsf{F} = dA$.

We further exploit the reality condition from Sec. B, and adopt a real gauge for the states $|u^a(\boldsymbol{k})\rangle$. Then $E \to B$ becomes a *real* vector bundle. To preserve the reality condition, from now on we consider only $\mathsf{O}(n)$ gauge transformations. As a consequence, the connection 1-form and the curvature 2-form take values in the orthogonal Lie group, $\mathfrak{so}(n)$. As these correspond to skew-symmetric matrices, the components of both of these objects are skew-symmetric in band indices. In particular, this implies that $\mathsf{F} = 0$, i.e. Berry curvature of a real Hamiltonian vanishes whenever well-defined. The "well-defined" condition fails only when the matrix of states $\mathfrak{U}$ is not a continuous function of $\boldsymbol{k}$, i.e. at band nodes. Indeed, band nodes of real Hamiltonians are known to carry a singular π-flux of the curvature.

While the change of Lie algebra $\mathfrak{u}(n) \to \mathfrak{so}(n)$ trivializes Berry curvature, it also enables *new* gauge-invariant and topological objects. Decomposing into the basis of 1-forms, $\mathcal{A} = \mathcal{A}_i dk^i$, the prefactors $\mathcal{A}_i$ are just skew-symmetric matrices. If we limit our attention to the case of an *even*, number n of bands, then we can define *Euler connection*

$$\mathrm{a} = \mathrm{Pf}(\mathcal{A}_i) dk^i \tag{23}$$

where Pf denotes Pfaffian. Below, we express the construction in Eq. (23) simply as "$\mathrm{a} = \mathrm{Pf}[\mathcal{A}]$". Recall that for antisymmetric matrix $\mathcal{M}$ and an arbitrary matrix X,

$$\mathrm{Pf}(X^\top \mathcal{M} X) = \det(X)\, \mathrm{Pf}(\mathcal{M}), \tag{24}$$

such that under $\mathsf{O}(n)$ transformations

$$\tilde{\mathrm{a}} = \det(X) \mathrm{a} + \mathrm{Pf}(X^\top dX) \tag{25}$$

with $\det(X) = \pm 1$, depending on whether we perform a proper or an improper orthogonal rotation.

Note that the Euler connection is *not* a matrix anymore, i.e. it can be treated as an ordinary differential 1-form. In particular, we can define the exterior derivative simply as

$$\mathrm{Eu} = d\mathrm{a} \tag{26}$$

which is a 2-form that we call *Euler curvature* or *Euler form*. Alternatively, we could decompose $\mathcal{F} = \mathcal{F}_{ij} dk^i \wedge dk^j$, where $\mathcal{F}_{ij}$ is a skew-symmetric matrix of numbers, and define

$$\mathrm{Eu} = \mathrm{Pf}(\mathcal{F}_{ij}) dk^i \wedge dk^j. \tag{27}$$

Furthermore, the expression $[\mathcal{A} \wedge \mathcal{A}]_{ij} = A_i A_j - A_j A_i$ in Eq. (19) has zero determinant, thus also vanishing Pfaffian. Therefore, the second definition of the Euler form together with Eq. (19) imply that $\mathrm{Eu} = \mathrm{Pf}(d\mathcal{A}) = d\,\mathrm{Pf}(\mathcal{A}) = d\mathrm{a}$, thus reproducing the definition in Eq. (26). Under gauge transformations,

$$\tilde{\mathrm{Eu}} = \det(X) \mathrm{Eu}, \tag{28}$$

meaning that the Euler form is invariant under proper $\mathsf{SO}(n)$ transformations of the n states, while it flips sign under improper $\mathsf{O}(n)$ transformations. We will refer to gauge transformations with $\det(X) = -1$ as *orientation-changing*.

If the rank of the bundle is $n = 2$, and the base space is two-dimensional and parameterized by momenta k_x and k_y, then the Euler curvature

$$\mathrm{Eu} = \left(\langle \partial_{k_x} u^1 | \partial_{k_y} u^2 \rangle - \langle \partial_{k_y} u^1 | \partial_{k_x} u^2 \rangle\right) dk^x \wedge dk^y, \quad (29)$$

is a single-component object. If further both the base space and the vector bundle are *orientable*, the Euler curvature can be treated as a volume form, and integrated over the base space B. Note that the nilpotence $d^2 = 0$ implies that the exterior derivative of the Euler curvature is zero. However, the potential may not be globally defined, therefore the Euler class of an oriented real bundle on a base space B defines an element of the de Rham cohomology $H^2_{\mathrm{dR}}(B)$. In fact, it can be shown [37] that $\frac{1}{2\pi}\mathrm{Eu}(\boldsymbol{k})$ integrates to an *integer* if the base space does not have a boundary, therefore the Euler form defines an element of the singular cohomology with *integer* coefficients, $H^2(B;\mathbb{Z})$ [36]. The integer

$$\chi(E) = \frac{1}{2\pi} \oint_B \mathrm{Eu} \quad (30)$$

is called the *Euler class* of the vector bundle E. The name is motivated by the observation that for a tangent bundle TM of a two-dimensional manifold M without a boundary, the integer $\chi(TM)$ reproduces the *Euler characteristic* of M [28]. This observation for $n = 2$ is a special case of the more general Chern-Gauss-Bonnet theorem [55], which applies to manifolds without boundary of higher even dimensions. Note also that the Euler characteristic of any odd-dimensional closed manifold is zero [56], thus justifying our motivation to consider real Hamiltonains with *even* number n of bands.

We remark that Eq. (30) is analogous to the definition of the first Chern number

$$c_1(E) = \frac{1}{2\pi} \oint_B \mathsf{F} \quad (31)$$

which is an element of $H^2(B;\mathbb{Z})$ for *complex* vector bundles. The mathematical arguments guaranteeing the quantization of $\chi(E)$ resp. $c_1(E)$ are essentially identical [36], and based on considering a covering of the base space B with open discs $\{\mathcal{D}_\alpha\}_{\alpha=1}^N$. To outline the argument, let us explicitly consider the case of B being a 2-sphere (S^2). The sphere is covered by $N = 2$ discs, e.g. the northern hemisphere $\mathcal{D}_{\mathrm{north}}$ and the southern hemisphere $\mathcal{D}_{\mathrm{south}}$, which meet at the equator $\gamma_{\mathrm{eq.}}$. Since disc is a contractible manifold, we can use Stokes' theorem to relate $\int_{\mathcal{D}_\alpha}\mathrm{Eu}$ to $\oint_{\partial\mathcal{D}_\alpha}\mathrm{a}$ (and analogously $\int_{\mathcal{D}_\alpha}\mathsf{F}$ to $\oint_{\partial\mathcal{D}_\alpha}A$ for the complex case) on each hemisphere. The resulting two integrals run around the equator in opposite directions, therefore

$$\begin{aligned} 2\pi\chi(E) = \oint_{S^2}\mathrm{Eu} &= \int_{\mathcal{D}_{\mathrm{north}}}\mathrm{Eu} + \int_{\mathcal{D}_{\mathrm{south}}}\mathrm{Eu} \\ &= \oint_{\gamma_{\mathrm{eq.}}}(\mathrm{a}_{\mathrm{north}} - \mathrm{a}_{\mathrm{south}}) = \oint_{\gamma_{\mathrm{eq.}}}\mathrm{Pf}[X^\top dX] \end{aligned} \quad (32)$$

where in the last expression we used that the connections $\mathrm{a}_{\mathrm{north}}$ and $\mathrm{a}_{\mathrm{south}}$ on the two hemispheres must be related by a gauge transformation [recall Eq. (25)], and we assumed that the orientation of the vector bundle is fixed on the whole 2-sphere [thus $\det(X) = +1$]. Note that if we write the $\mathsf{SO}(2)$ matrix X using the algebra element $\alpha \in \mathfrak{so}(2)$ as $X = \mathrm{e}^{+\mathrm{i}\alpha\sigma_y}$, then the last expression in Eq. (32) reduces to integration of $\mathrm{Pf}[X^\top dX] = d\alpha$. Since the gauge transformation X must return to its original form after traversing the equator, the value of α must increase by an integer multiple of 2π on $\gamma_{\mathrm{eq.}}$. Therefore

$$2\pi\chi(E) = \oint_{\gamma_{\mathrm{eq.}}} d\alpha = 2\pi m \quad \text{with } m \in \mathbb{Z} \quad (33)$$

which completes the proof of the quantization of the Euler form for real orientable vector bundles on S^2.

D. Euler form in three-band models

In this section, we further elaborate on the analogy between the Euler class and the first Chern number by briefly focusing on the minimal models. More specifically, we show that both the Berry curvature $\mathsf{F}(\boldsymbol{k})$ of one band obtained from a two-band complex Hamiltonian, as well as the Euler form $\mathrm{Eu}(\boldsymbol{k})$ of two bands obtained from a three-band real Hamiltonian, can be understood by considering geometry on a 2-sphere (S^2). The discussion below thus proves the geometric interpretation of Euler form presented in Fig. 4(b) of the main text. We note that this section provides a slight digression from the theoretical notions presented in previous sections and we return to the general case of real models with an arbitrary number of bands.

Let us first recall the mathematics behind the first Chern number of a complex Hamiltonian, defined in Eq. (31), for the case of two bands. Hermitian two-band Hamiltonians can be decomposed using the Pauli matrices and the unit matrix as

$$H(\boldsymbol{k}) = \boldsymbol{h}(\boldsymbol{k}) \cdot \boldsymbol{\sigma} + h_0(\boldsymbol{k})\mathbb{1} \quad (34)$$

where $h_{0,x,y,z}(\boldsymbol{k})$ are real functions of momentum. Spectral flattening brings eigenvalues of the Hamiltonian to ± 1 without changing the band topology [6], and is associated with replacing $h_0 \mapsto 0$ and $\boldsymbol{h} \mapsto \boldsymbol{h}/||\boldsymbol{h}|| \equiv \boldsymbol{n}$. The band topology of the two-band complex Hamiltonian is thus completely captured by the three-component unit vector $\boldsymbol{n}(\boldsymbol{k}) \in S^2$. It is known [2, 3] that the Berry cur-

vature of one of the two bands can be expressed as

$$\mathsf{F}_{ij} = \tfrac{1}{2}\boldsymbol{n}\cdot(\partial_{k_i}\boldsymbol{n}\times\partial_{k_j}\boldsymbol{n}), \tag{35}$$

such that $\mathsf{F}_{ij}\,dk_i\,dk_j$ corresponds to one half of the (oriented) solid angle spanned by $\boldsymbol{n}$ on the S^2 as the momentum argument is varied over a rectangle of size $\mathrm{d}k_i\times\mathrm{d}k_j$. For a *closed* two-dimensional base manifold, the vector $\boldsymbol{n}$ has to wrap around the unit sphere an integer number of times, hence the integral of $\mathsf{F}_{ij}\,dk_i\,dk_j$, i.e. the total (oriented) solid angle spanned by $\boldsymbol{n}$, must be quantized to integer multiples of 2π. Therefore, $c_1(E)$ defined in Eq. (31) is an integer. This simple argument does not generalize to models with more than two bands, in which case one has to follow the proof outlined at the end of Sec. C.

We find that a very similar geometric interpretation also applies to Euler form of two bands obtained from a three-band real Hamiltonian. In this case, spectral flattening brings the Hamiltonian with two occupied bands and one unoccupied band to [26]

$$H(\boldsymbol{k}) = \boldsymbol{n}(\boldsymbol{k})\cdot\boldsymbol{n}(\boldsymbol{k})^{\top} - 2\cdot\mathbb{1}, \tag{36}$$

where $\boldsymbol{n}(\boldsymbol{k}) = \boldsymbol{u}^1(\boldsymbol{k})\times\boldsymbol{u}^2(\boldsymbol{k}) \in S^2$ is the (normalized) column vector representing the unoccupied state, which can be represented as cross product of the (normalized) occupied states $\boldsymbol{u}^1(\boldsymbol{k})$ and $\boldsymbol{u}^2(\boldsymbol{k})$. Note that, because of the reality condition, the left ("bra") and the right ("ket") eigenstates are componentwise equal to each other. The quadratic dependence of the Hamiltonian on the unit vector, manifest in Eq. (36), implies that vectors $\pm\boldsymbol{n}$ represent the same Hamiltonian. Therefore the space of *unique* spectrally flattened 3-band Hamiltonians is $S^2/\mathbb{Z}_2 \equiv \mathbb{R}P^2$ [18]. However, if the vector bundle defined by $H(\boldsymbol{k})$ is orientable (which is a necessary condition to define Euler form), then there are no closed paths $\gamma\subset B$ in the base manifold which would be mapped by the Hamiltonian to the non-contractible path in $\mathbb{R}P^2$. Therefore, Euler form of an *orientable* rank-2 bundle obtained from a three-band real Hamiltonian, is related to geometry on S^2. In fact, we show below that

$$\mathrm{Eu}_{ij} = \boldsymbol{n}\cdot\left(\partial_{k_i}\boldsymbol{n}\times\partial_{k_j}\boldsymbol{n}\right), \tag{37}$$

which [besides the altered interpretation of $\boldsymbol{n}(\boldsymbol{k})$] qualitatively differs from Eq. (35) only in the absence of the prefactor $\frac{1}{2}$. Following the same arguments as for the first Chern number, we find that for three-band models the Euler class $\chi(E)$ defined in Eq. (30) must be an *even* integer. This agrees with the known fact, that odd values of the Euler class (corresponding to a non-trivial second Stiefel-Whitney class) require models with at least two occupied and with at least two unoccupied bands [20]. We also remark that the cross-product definition of $\boldsymbol{n}(\boldsymbol{k})$ in terms of the two occupied states makes the expression in Eq. (37) invariant only under the *proper* $\mathsf{SO}(2)$ gauge transformations of the occupied states, reminding us of the importance of orientability of the vector bundle.

The remainder of this section contains a proof of Eq. (37). While the logic of the proof is straightforward, some of the expressions are rather lengthy. We employ the Einstein summation convention, and we write

$$n_a = \epsilon_{abc}u^1_b u^2_c \tag{38}$$

where ϵ is the Levi-Civita symbol. The right-hand side of Eq. (37) can be expressed as

$$(37) = \epsilon_{abc}u^1_b u^2_c \epsilon_{ade}\partial_{k_i}(\epsilon_{dfg}u^1_f u^2_g)\partial_{k_j}(\epsilon_{ehi}u^1_h u^2_i). \tag{39}$$

Using the identity $\epsilon_{abc}\epsilon_{ade} = \delta_{bd}\delta_{ce} - \delta_{be}\delta_{cd}$, and performing the summation over indices b and c, we obtain

$$(37) = \epsilon_{dfg}\epsilon_{ehi}(u^1_d u^2_e - u^1_e u^2_d)\partial_{k_i}(u^1_f u^2_g)\partial_{k_j}(u^1_h u^2_i). \tag{40}$$

To get rid off the remaining Levi-Civita symbols, we use

$$\epsilon_{dfg}\epsilon_{ehi} = \delta_{de}(\delta_{fh}\delta_{gi} - \delta_{fi}\delta_{gh}) - \delta_{dh}(\delta_{fe}\delta_{gi} - \delta_{fi}\delta_{ge}) + \delta_{di}(\delta_{fe}\delta_{gh} - \delta_{fh}\delta_{ge}). \tag{41}$$

This long identity has to be substituted into Eq. (40). Note that the combinations of Kronecker symbols containing δ_{de} trivially lead to zero after the substitution, because $\delta_{de}(u^1_d u^2_e - u^1_e u^2_d) = 0$. The remaining terms in Eq. (41), after summing over indices e, h, and i, lead to

$$\begin{aligned}(37) = &-(u^1_d u^2_f - u^1_f u^2_d)\partial_{k_i}(u^1_f u^2_g)\partial_{k_j}(u^1_d u^2_g) + (u^1_d u^2_g - u^1_g u^2_d)\partial_{k_i}(u^1_f u^2_g)\partial_{k_j}(u^1_d u^2_f)\\ &+(u^1_d u^2_f - u^1_f u^2_d)\partial_{k_i}(u^1_f u^2_g)\partial_{k_j}(u^1_g u^2_d) - (u^1_d u^2_g - u^1_g u^2_d)\partial_{k_i}(u^1_f u^2_g)\partial_{k_j}(u^1_f u^2_g)\end{aligned} \tag{42}$$

Performing the derivatives by parts, Eq. (42) expands into 32 individual terms

$$
\begin{aligned}
(37) = &-u^1_d u^2_f (\partial_{k_i} u^1_f) u^2_g (\partial_{k_j} u^1_d) u^2_g - u^1_d u^2_f (\partial_{k_i} u^1_f) u^2_g u^1_d (\partial_{k_j} u^2_g) - u^1_d u^2_f u^1_f (\partial_{k_i} u^2_g)(\partial_{k_j} u^1_d) u^2_g - u^1_d u^2_f u^1_f (\partial_{k_i} u^2_g) u^1_d (\partial_{k_j} u^2_g) \\
&+u^1_f u^2_d (\partial_{k_i} u^1_f) u^2_g (\partial_{k_j} u^1_d) u^2_g + u^1_f u^2_d (\partial_{k_i} u^1_f) u^2_g u^1_d (\partial_{k_j} u^2_g) + u^1_f u^2_d u^1_f (\partial_{k_i} u^2_g)(\partial_{k_j} u^1_d) u^2_g + u^1_f u^2_d u^1_f (\partial_{k_i} u^2_g) u^1_d (\partial_{k_j} u^2_g) \\
&+u^1_d u^2_g (\partial_{k_i} u^1_f) u^2_g (\partial_{k_j} u^1_d) u^2_f + u^1_d u^2_g (\partial_{k_i} u^1_f) u^2_g u^1_d (\partial_{k_j} u^2_f) + u^1_d u^2_g u^1_f (\partial_{k_i} u^2_g)(\partial_{k_j} u^1_d) u^2_f + u^1_d u^2_g u^1_f (\partial_{k_i} u^2_g) u^1_d (\partial_{k_j} u^2_f) \\
&-u^1_g u^2_d (\partial_{k_i} u^1_f) u^2_g (\partial_{k_j} u^1_d) u^2_f - u^1_g u^2_d (\partial_{k_i} u^1_f) u^2_g u^1_d (\partial_{k_j} u^2_f) - u^1_g u^2_d u^1_f (\partial_{k_i} u^2_g)(\partial_{k_j} u^1_d) u^2_f - u^1_g u^2_d u^1_f (\partial_{k_i} u^2_g) u^1_d (\partial_{k_j} u^2_f) \\
&+u^1_d u^2_f (\partial_{k_i} u^1_f) u^2_g (\partial_{k_j} u^1_g) u^2_d + u^1_d u^2_f (\partial_{k_i} u^1_f) u^2_g u^1_g (\partial_{k_j} u^2_d) + u^1_d u^2_f u^1_f (\partial_{k_i} u^2_g)(\partial_{k_j} u^1_g) u^2_d + u^1_d u^2_f u^1_f (\partial_{k_i} u^2_g) u^1_g (\partial_{k_j} u^2_d) \\
&-u^1_f u^2_d (\partial_{k_i} u^1_f) u^2_g (\partial_{k_j} u^1_g) u^2_d - u^1_f u^2_d (\partial_{k_i} u^1_f) u^2_g u^1_g (\partial_{k_j} u^2_d) - u^1_f u^2_d u^1_f (\partial_{k_i} u^2_g)(\partial_{k_j} u^1_g) u^2_d - u^1_f u^2_d u^1_f (\partial_{k_i} u^2_g) u^1_g (\partial_{k_j} u^2_d) \\
&-u^1_d u^2_g (\partial_{k_i} u^1_f) u^2_g (\partial_{k_j} u^1_f) u^2_d - u^1_d u^2_g (\partial_{k_i} u^1_f) u^2_g u^1_f (\partial_{k_j} u^2_d) - u^1_d u^2_g u^1_f (\partial_{k_i} u^2_g)(\partial_{k_j} u^1_f) u^2_d - u^1_d u^2_g u^1_f (\partial_{k_i} u^2_g) u^1_f (\partial_{k_j} u^2_d) \\
&+u^1_g u^2_d (\partial_{k_i} u^1_f) u^2_g (\partial_{k_j} u^1_f) u^2_d + u^1_g u^2_d (\partial_{k_i} u^1_f) u^2_g u^1_f (\partial_{k_j} u^2_d) + u^1_g u^2_d u^1_f (\partial_{k_i} u^2_g)(\partial_{k_j} u^1_f) u^2_d + u^1_g u^2_d u^1_f (\partial_{k_i} u^2_g) u^1_f (\partial_{k_j} u^2_d)
\end{aligned}
$$

Most of these 32 terms vanish. To see this, we use orthonormality $u^1_a u^2_a = 0$ on the vector coordinates displayed in red. Furthermore, the normalization $u^1_a u^1_a = 1 = u^2_a u^2_a$ implies that $u^1_a(\partial_{k_\beta} u^1_a) = 0 = u^2_a(\partial_{k_\beta} u^2_a)$, which we indicate in blue. Only two terms remain, in which we further use the normalization to 1 on vector components displayed in green. After renaming the repeated indices, we obtain

$$
\mathrm{Eu}_{ij} = (\partial_{k_i} u^1_f)(\partial_{k_j} u^2_f) - (\partial_{k_j} u^1_f)(\partial_{k_i} u^2_f) \equiv \langle \partial_{k_i} u^1 | \partial_{k_j} u^2 \rangle - \langle \partial_{k_j} u^1 | \partial_{k_i} u^2 \rangle . \tag{43}
$$

The last expression exactly corresponds to the components of the the Euler form over two bands as defined in Eq. (29). This completes the proof of Eq. (37).

E. Singularity of Euler form at principal nodes.

In the main text we consider the Euler form $\mathrm{Eu}(\boldsymbol{k})$ defined by the two principal bands. Note that adjacent nodes pose problems for the mathematical construction. This is because circumnavigating an adjacent node reverses the orientation of one of the principal Bloch states (the one that participates in the formation of the node), but not the other one. Therefore, parallel transport around an adjacent node is associated with an *improper* gauge transformation $X = \sigma_z \notin \mathsf{SO}(2)$. Since such vector bundle is not orientable, its Euler curvature cannot be defined. This is the reason why we only consider calculations over regions with no adjacent nodes.

On the other hand, the behavior of the Euler form near a *principal* node is more subtle. First, circumnavigating a principal node reverses the sign of *both* principal Bloch states, which corresponds to a *proper* gauge transformation $X = -\mathbb{1} \in \mathsf{SO}(2)$, such that Euler form of the bundle is well-defined on an annulus around the node. On the other hand, the eigenstates of the Hamiltonian are not continuous functions of $\boldsymbol{k}$ at the location of principal nodes, suggesting that the derivatives of the eigenstates are ill-defined at these points. Nevertheless, we show that the bundle spanned by the two principal bands is actually continuous and differentiable at principal nodes. The last two statements are not in contradiction! Indeed, a discontinuous basis on the bundle does not imply discontinuity of the bundle. There may be (and we show that there really is) a different basis which is perfectly continuous at principal nodes.

However, one has to consider the relevance of the two bases for physical observables. Since the two principal bands are separated by a band gap away from the principal nodes, the discontinuous basis spanned by the principal eigenstates has a special physical significance. Especially, we show in Sec. F that this canonical (although discontinuous) basis encodes observable features, such as the path-dependent ability of band nodes to annihilate. This information is lost once we allow for mixing of the two principal eigenstates by a general $\mathsf{SO}(2)$ gauge transformation – such as when going to the basis that reveals the continuity of the bundle. These are subtle but important issues, which we discuss in more detail in Sec. F.

In contrast, the present section is only concerned with the analytic properties of the vector bundle spanned by the principal bands in the two different choices of a basis. We begin our discussion by presenting the most general Hamiltonian near a principal node to the linear order in momentum. We treat the obtained Hamiltonian perturbatively, and we first consider the *eigenstate basis* to reveal the ill-defined structure of the Euler form near the principal node. Understanding the Euler form in the eigenstate basis is important, both because of its physical significance but also because it is the most natural basis to use in numerical calculations, as presented later in Sec. H. We subsequently show that it is possible to construct a mixture of the two principal states that is continuous and differentiable at the node, thus leading to a continuous Euler form at the node. The bottom line of our analysis, important for the discussion in Secs. F–H, can be stated as follows. *If one describes the vector bundle spanned by the two principal bands using the eigenstate basis, then the Euler form is bounded (which allows us to integrate it) but not differentiable (which prevents us from a naïvely applying Stokes' theorem) at principal nodes.*

Let us proceed with the actual analytic calculations.

We first consider a two-band model that exhibits a node at $\boldsymbol{k}=\boldsymbol{0}$ at zero energy. To linear order, the Hamiltonian near the node must take the form

$$\mathcal{H}_{\text{2-band}}(\boldsymbol{k}) = \sum_{i=1}^{2}\sum_{j=0}^{3} k_i h_{ij} \sigma_j \tag{44}$$

where $k_{1,2}$ are the two momentum coordinates, h_{ij} are 8 real coefficients, and $\{\sigma_j\}_{j=0}^{3}$ is the unit matrix and the three Pauli matrices. It is known that by a suitable proper rotation and by a linear rescaling of the momentum coordinates to $\boldsymbol{\kappa}(\boldsymbol{k})$, we can bring the Hamiltonian to the form

$$\mathcal{H}_{\text{2-band}}(\boldsymbol{\kappa}) = \begin{pmatrix} \kappa_1 + \varepsilon(\boldsymbol{\kappa}) & \pm\kappa_2 \\ \pm\kappa_2 & -\kappa_1 + \varepsilon(\boldsymbol{\kappa}) \end{pmatrix}, \tag{45}$$

where $\varepsilon(\boldsymbol{\kappa}) = v_1\kappa_1 + v_2\kappa_2$ describes the tilting of the band node [39]. Since the considered coordinate transformation is linear, the associated Jacobian $J_{ij} = \partial\kappa_i/\partial k_j$ is a constant matrix. The $\pm$ sign corresponds to nodes with positive vs. negative winding number $w \in \pi_1[\mathsf{SO}(2)] = \mathbb{Z}$, and we keep it unspecified throughout the whole section.

If there are additional bands, then the same rotation of the two basis vectors brings the corresponding n-band linear-order Hamiltonian to the form

$$\mathcal{H}_{n\text{-band}}(\boldsymbol{\kappa}) = \begin{pmatrix} \kappa_1+\varepsilon(\boldsymbol{\kappa}) & \pm\kappa_2 & f^\top(\boldsymbol{\kappa}) \\ \pm\kappa_2 & -\kappa_1+\varepsilon(\boldsymbol{\kappa}) & g^\top(\boldsymbol{\kappa}) \\ f(\boldsymbol{\kappa}) & g(\boldsymbol{\kappa}) & \mathcal{E}+h(\boldsymbol{\kappa}) \end{pmatrix}, \tag{46}$$

where $f(\boldsymbol{\kappa})$ and $g(\boldsymbol{\kappa})$ are $\boldsymbol{\kappa}$-linear $(n-2)$-component column vectors with real components $\{f_c(\boldsymbol{\kappa})\}_{c=3}^{n}$ and $\{g_c(\boldsymbol{\kappa})\}_{c=3}^{n}$, $\mathcal{E}$ is a non-degenerate diagonal matrix of $(n-2)$ non-zero band energies, and $h(\boldsymbol{\kappa})$ is $\boldsymbol{\kappa}$-linear Hermitian matrix of size $(n-2)\times(n-2)$. In Eq. (46) we explicitly assume that the additional $(n-2)$ basis vectors of the Hilbert space are given by the additional eigenstates of the Hamiltonian at the node, therefore $h(\boldsymbol{\kappa}=\boldsymbol{0}) = \mathbb{0}$. Therefore, after adopting the properly rotated and rescaled momentum coordinates and the right Hilbert-space basis, the model in Eq. (46) represents the *most general* n-band real Hamiltonian near a principal node to linear order in momentum.

Our incentive is to find the approximate form of the principal Bloch vectors near the principal band node of the model in Eq. (46) using perturbation theory. Then we can use the perturbative result to study the behavior of the Euler form near the principal node. Our goal is to examine whether the lowest order of the Euler form contains a $1/|\boldsymbol{\kappa}|$ divergence, or a discontinuity, or whether it is perfectly regular. As already advertised, we find that the result of the analysis depends on the choice of basis of the bundle.

To proceed, we split the Hamiltonian in Eq. (46) into $\mathcal{H}_0 = \mathrm{diag}(\epsilon(\boldsymbol{\kappa}), \epsilon(\boldsymbol{\kappa}), \mathcal{E})$, and a "perturbation" $\mathcal{H}'$ that contians all the terms linear in $\boldsymbol{\kappa}$, that is

$$\mathcal{H}'(\boldsymbol{\kappa}) = \begin{pmatrix} \kappa_1 & \pm\kappa_2 & f^\top(\boldsymbol{\kappa}) \\ \pm\kappa_2 & -\kappa_1 & g^\top(\boldsymbol{\kappa}) \\ f(\boldsymbol{\kappa}) & g(\boldsymbol{\kappa}) & h(\boldsymbol{\kappa}) \end{pmatrix}. \tag{47}$$

The first step of the pertubation theory requires us to find states that diagonalize the matrix $\mathcal{H}'_{ab} = \langle a|\,\mathcal{H}'\,|b\rangle$ with $a,b\in\{1,2\}$ representating the degenerate states at the principal nodes. We take $|1\rangle = (1\ 0\ 0\ \ldots)^\top$ and $|2\rangle = (0\ 1\ 0\ \ldots)^\top$, in which case this matrix corresponds simply to the upper-left 2×2 block of Eq. (47). If we further decompose $\boldsymbol{\kappa}$ using the polar coordinates as $\kappa_1 = \kappa\cos\phi$ and $\kappa_2 = \kappa\sin\phi$, this block is diagonalized by

$$\left|1^{(0)}\right\rangle = \begin{pmatrix} \pm\sin\frac{\phi}{2} \\ -\cos\frac{\phi}{2} \\ \boldsymbol{0} \end{pmatrix} \text{ and } \left|2^{(0)}\right\rangle = \zeta\begin{pmatrix} +\cos\frac{\phi}{2} \\ \pm\sin\frac{\phi}{2} \\ \boldsymbol{0} \end{pmatrix} \tag{48}$$

where $\zeta = \pm 1$ corresponds to two different orientations of the bundle. Changing the relative sign between the two states corresponds to orientation-changing gauge transformation $X = \pm\sigma_z$. On the other hand, increasing $\phi \mapsto \phi + 2\pi$ flips the sign of *both* bands, which corresponds to a proper gauge transformation $X = -\mathbb{1}$.

The first-order correction to the states in Eq. (48) is given by

$$|a^{(1)}\rangle = \sum_{c=3}^{n} \frac{\langle c|\,\mathcal{H}'\,|a^{(0)}\rangle}{\epsilon(\boldsymbol{\kappa}) - \mathcal{E}_c}\,|c\rangle \tag{49}$$

where $|c\rangle$ is the c^{th} element of the basis in which we expressed Eq. (47). This prescription does not lead to a change in the first two compoments of the principal vectors, while for compoments with $c\geq 3$ we find

$$\langle c|1^{(1)}\rangle = \tfrac{1}{\varepsilon(\boldsymbol{\kappa})-\mathcal{E}_c}\left[\pm f_c(\boldsymbol{\kappa})\sin\tfrac{\phi}{2} - g_c(\boldsymbol{\kappa})\cos\tfrac{\phi}{2}\right] \tag{50}$$

$$\langle c|2^{(1)}\rangle = \tfrac{\zeta}{\varepsilon(\boldsymbol{\kappa})-\mathcal{E}_c}\left[+f_c(\boldsymbol{\kappa})\cos\tfrac{\phi}{2} \pm g_c(\boldsymbol{\kappa})\sin\tfrac{\phi}{2}\right]. \tag{51}$$

Note that the expressions inside the square brackets are linear in $\boldsymbol{\kappa}$, while the prefactor can be approximated for $\boldsymbol{\kappa}$ close to $\boldsymbol{0}$ as

$$\frac{1}{\varepsilon(\boldsymbol{\kappa})-\mathcal{E}_c} \approx -\frac{1}{\mathcal{E}_c} + \frac{v_1\kappa_1 + v_2\kappa_2}{\mathcal{E}_c^2}. \tag{52}$$

Therefore, if we are after terms of the lowest order in $\boldsymbol{\kappa}$, we can approximate the prefactor simply by $-1/\mathcal{E}_c$. Furthermore, notice that states $\left|1^{(0+1)}\right\rangle$ and $\left|2^{(0+1)}\right\rangle$, which we obtained by performing the first-order perturbation theory, are not properly normalized. However, since the lowest-order corrections $\left|1^{(1)}\right\rangle$ and $\left|2^{(1)}\right\rangle$ are *linear* in $\boldsymbol{\kappa}$, the correction from the proper normalization would be *quadratic* in $\boldsymbol{\kappa}$. More explicitly, normalizing the states would induce a prefactor of the form

$$\frac{1}{\sqrt{1+||\boldsymbol{\kappa}\mathcal{N}||^2}} \approx 1 - \frac{1}{2}||\boldsymbol{\kappa}\mathcal{N}||^2 \tag{53}$$

where $||\boldsymbol{\kappa}\mathcal{N}||$ represents the normalization of the first-order correction. Since we are interested only in corrections to the principal states of the *lowest order* in $\boldsymbol{\kappa}$, we safely ignore the normalization.

We have established the lowest-order (linear) corrections in $\boldsymbol{\kappa}$ to the principal Bloch states in Eq. (48). We can use the obtained states to calculate the Euler connection and the Euler form *in the eigenstate basis*,

$$\mathrm{a}_i = \langle 1|\partial_{\kappa_i} 2\rangle \quad \text{and} \quad \mathrm{Eu} = \langle \partial_{\kappa_1} 1|\partial_{\kappa_2} 2\rangle - \langle \partial_{\kappa_2} 1|\partial_{\kappa_1} 2\rangle \tag{54}$$

where we dropped the superscript "$^{(0+1)}$" for brevity. To calculate the derivatives, note that

$$\partial_{\kappa_1} = \frac{\partial\kappa}{\partial\kappa_1}\partial_\kappa + \frac{\partial\phi}{\partial\kappa_1}\partial_\phi = \cos\phi\partial_\kappa - \frac{\sin\phi}{\kappa}\partial_\phi \tag{55}$$

$$\partial_{\kappa_2} = \frac{\partial\kappa}{\partial\kappa_2}\partial_\kappa + \frac{\partial\phi}{\partial\kappa_2}\partial_\phi = \sin\phi\partial_\kappa + \frac{\cos\phi}{\kappa}\partial_\phi. \tag{56}$$

The existence of the $1/\kappa$ factors in these expressions suggests that we might encounter a singularity as we approach the principal node. Finally, to complete the calculation we also rewrite

$$f_c(\boldsymbol{\kappa}) = \alpha_c\kappa\cos\phi + \beta_c\kappa\sin\phi \tag{57}$$

$$g_c(\boldsymbol{\kappa}) = \gamma_c\kappa\cos\phi + \delta_c\kappa\sin\phi. \tag{58}$$

With the help of `Mathematica`, we find the Euler connection to the leading order in κ as

$$\mathbf{a} = \frac{\pm\zeta}{2\kappa}(\sin\phi, -\cos\phi) + \mathcal{O}(\kappa) \tag{59}$$

which *diverges* as we approach the node. In contrast, the Euler form to the leading order in κ is

$$\mathrm{Eu} = -\zeta\sum_{c=3}^{n}\frac{1}{\mathcal{E}_c^2}\Big[(\beta_c\gamma_c - \alpha_c\delta_c) \pm \tfrac{1}{2}(\alpha_c\cos\phi + \beta_c\sin\phi)^2 \pm \tfrac{1}{2}(\gamma_c\cos\phi + \delta_c\sin\phi)^2\Big] \tag{60}$$

which *does not diverge* at the node. All the $1/\kappa$ factors, present in some of the previous formulae, cancel out. Substituting back the original coordinates, $\boldsymbol{\kappa} \to \boldsymbol{k}$, corresponds to a double multiplication by the (constant) Jacobian matrix, which also does not induce a divergence. Furthermore, we already argued that higher-order contributions to $\mathrm{Eu}(\boldsymbol{\kappa})$ cannot induce a divergence as $\boldsymbol{\kappa} \to \mathbf{0}$. Altogether, we find that the Euler form in the eigenstates basis is *bounded* near a principal node. Note, however, that the dependence of Eu on ϕ (which persists for $\kappa \to 0$) implies that Eu is *discontinuous* at $\boldsymbol{k} = \mathbf{0}$. In particular, the discontinuity implies that the Euler form is not differentiable at principal nodes, which poses an obstruction for the use of Stokes' theorem on regions that contain principal nodes.

We now show that the vector bundle spanned by the two principal eigenstates is continuous at the principal node. Recall, that a rank-2 bundle is a collection of two-dimensional planes – one plane per every point of the base space. The orientation of these planes varies between the points of the base. Importantly, these planes need not in general be equipped with any intrinsic basis. The basis vectors that we use to span these planes are just an auxiliary tool. Performing an $\mathsf{SO}(2)$ gauge transformation on the two vectors spanning the rank-2 bundle does not correspond to a change of the bundle, just to a *change of coordinates* that we use to describe the bundle.

In particular, it is convenient to consider the "mixed" states

$$|A(\boldsymbol{\kappa})\rangle = \pm\sin\tfrac{\phi}{2}\left|1^{(0+1)}\right\rangle + \zeta\cos\tfrac{\phi}{2}\left|2^{(0+1)}\right\rangle \tag{61}$$

$$|B(\boldsymbol{\kappa})\rangle = -\zeta\cos\tfrac{\phi}{2}\left|1^{(0+1)}\right\rangle \pm \sin\tfrac{\phi}{2}\left|2^{(0+1)}\right\rangle \tag{62}$$

which are related to the eigenstates of the perturbed Hamiltonian by a proper gauge transformation

$$X(\boldsymbol{\kappa};\zeta) = \begin{pmatrix} \pm\sin\frac{\phi}{2} & +\zeta\cos\frac{\phi}{2} \\ -\zeta\cos\frac{\phi}{2} & \pm\sin\frac{\phi}{2} \end{pmatrix} \tag{63}$$

Using trigonometric identities, we find that to linear order in $\boldsymbol{\kappa}$ these rotated vectors are

$$|A(\boldsymbol{\kappa})\rangle = \begin{pmatrix} 1 \\ 0 \\ \{\frac{-f_c}{\mathcal{E}_c}\}_{c=3}^{n} \end{pmatrix} \quad |B(\boldsymbol{\kappa})\rangle = \zeta\begin{pmatrix} 0 \\ 1 \\ \{\frac{-g_c}{\mathcal{E}_c}\}_{c=3}^{n} \end{pmatrix}. \tag{64}$$

These are manifestly *continuous* at $\boldsymbol{\kappa} \to \mathbf{0}$, meaning that the vector bundle spanned by the two principal bands is continuous at the principal node. In fact, the bundle is *differentiable* at $\boldsymbol{k} = \mathbf{0}$, which is best appreciated by considering $n = 3$, in which case the rank-2 bundle can be described by the vector spanning its rank-1 complement inside the 3-dimensional real Hilbert space, which we construct as a cross product

$$|A(\boldsymbol{\kappa})\rangle \times |B(\boldsymbol{\kappa})\rangle = \left(\frac{f_3(\boldsymbol{\kappa})}{\mathcal{E}_3}\,,\ \frac{g_3(\boldsymbol{\kappa})}{\mathcal{E}_3}\,,\ 1\right)^\top \tag{65}$$

Especially, we find the the Euler connection and the Euler form to the leading order in κ *in the continuous basis* as

$$\tilde{\mathbf{a}} = \langle A|\boldsymbol{\nabla}B\rangle = \frac{\zeta\,(\alpha_3 k_x + \beta_3 k_y)}{\mathcal{E}_3^2}(\gamma_3, \delta_3) \tag{66}$$

and

$$\tilde{\mathrm{Eu}} = \langle\partial_1 A|\partial_2 B\rangle - \langle\partial_2 A|\partial_1 B\rangle = -\frac{\zeta}{\mathcal{E}_3^2}(\beta_3\gamma_3 - \alpha_3\delta_3) \tag{67}$$

which are both perfectly regular for $\boldsymbol{\kappa} \to \mathbf{0}$. In particular, the result in Eq. (67) exactly reproduces the ϕ-*independent* contribution to Eq. (60).

How is the difference between the results in Eqs. (60) and (67) compatible with the fact, stated in Sec. C, that the Euler form is invariant under proper gauge transformations? The subtlety lies in the fact, that the proof of gauge invariance of $\mathrm{Eu}(\boldsymbol{\kappa})$ assumes a *differentiable* gauge transformation $X(\boldsymbol{\kappa})$. This is not fulfilled by the trans-

formation in Eq. (63) at $\boldsymbol{\kappa} = \mathbf{0}$, thus allowing us to change the behaviour of the Euler form at that point. Furthermore, note that the very definition of the Euler form as the Pfaffian of the Berry-Wilczek-Zee connection requires the collection of states $\mathfrak{U}(\boldsymbol{\kappa})$ itself to be differentiable, else the exterior derivatives in Eqs. (16) and (19) are meaningless. But this assumption is not fulfilled by the states specified in Eqs. (48–51) at $\boldsymbol{\kappa} = \mathbf{0}$. Therefore, our original calculation of the Euler form at the principal node has been flawed to begin with. The reason that the gauge transformation in Eq. (63) suddenly made the Euler form at $\boldsymbol{\kappa} \to \mathbf{0}$ regular is precisely that the rotated states $|A(\boldsymbol{\kappa})\rangle$ and $|B(\boldsymbol{\kappa})\rangle$ are differentiable at that point.

Nevertheless, in spite of the nicer analytic properties of Euler form in the smooth basis, one should keep in mind the *physical significance* of the eigenstate basis. In other words, the physical setting makes the considered vector bundle equipped with a canonical (albeit discontinuous) basis! We analyze the importance of this special basis for physical observables in the next section.

F. Euler class for manifolds with a boundary

In this section, we generalize the notion of Euler class of a pair of principal bands in two important ways. First, we consider a base manifold *with a boundary*. Throughout the discussion, we explicitly assume that the manifold is topologically a *disc* (denoted $\mathcal{D}$), which has boundary homeomorphic to a circle ($\partial\mathcal{D} \simeq S^1$). Nevertheless, most of the presented results readily generalize to arbitrary manifolds with a boundary as long as the vector bundle spanned by the principal bunds remains orientable. Second, we admit the occurrence of principal nodes inside the base manifold. Crucially, to obtain useful information from such a generalization, it is essential to *adopt the eigenstate basis*. We find that the value of the Euler class on a disc $\mathcal{D}$, denoted $\chi(\mathcal{D})$, indicates whether the collection of principal nodes can annihilate inside $\mathcal{D}$.

The first generalization is straightforward. If there are no band nodes in $\mathcal{D}$, then the eigenstate basis is continuous. Therefore, Stokes' theorem guarantees that

$$\chi(\mathcal{D}) = \frac{1}{2\pi}\left(\int_{\mathcal{D}} \mathrm{Eu} - \oint_{\partial\mathcal{D}} \mathrm{a}\right) = 0 \quad \text{(if no nodes in } \mathcal{D}\text{)} \quad (68)$$

is invariant. Let us further assume the presence of principal nodes in $\mathcal{D}$ (but no adjacent nodes as we want the bundle to remain orientable). We proved in the second part of Sec. E that the vector bundle spanned by the two principal bands is continuous everywhere, including at the nodes. However one has to depart from the eigenstate basis to reveal this fact, and instead has to consider the "mixed" basis, cf. Eqs. (61–67). In such *continuous basis*, Stokes' theorem still applies, which implies the validity of Eq. (68) even in the presence of principal nodes. One concedes that the vector bundle spanned by the two principal bands on a disc cannot support a non-trivial topological invariant.

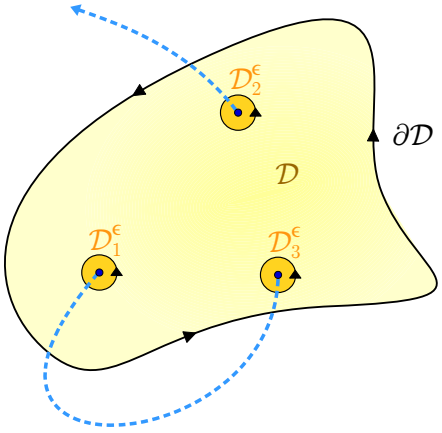

FIG. S-7. Illustration of the use of Stokes' theorem as discussed in the text. Region $\mathcal{D}$ is the disc on which we study the real orientable vector bundle, and the blue dots are the principal nodes. We apply Stokes' theorem to $\mathcal{D}\setminus\cup_\alpha \mathcal{D}_\alpha^\epsilon$, i.e. to the region with tiny discs around the nodes cut out. The blue dashed lines represent Dirac strings. Only the end-points of Dirac strings are physically meaningful. In the case of the eigenstate basis the Dirac string end-points coincides with principal nodes, whereas a gauge transformation that reguralizes the nodes creates a new Dirac string that exactly compensates the singular behavior.

However, one should keep in mind the *physical realization* of the vector bundle as a pair of energy bands that are non-degenerate away from the band nodes. This interpretation equips the bundle with a canonical basis, namely the *eigenstate basis* discussed at length in the first part of Sec. E. Therefore, one should only consider deformations of the vector bundle which preserve this additional structure. Indeed, we show below that such constraint allows for a subtly modified definition of $\chi(\mathcal{D})$, which constitutes a *half-integer* topological invariant.

To develop the generalization of the Euler class, one should first recognize that each principal node is associated with a Dirac string [35]. Returning back to Eqs. (48–51), we observe that the continuous real gauge for eigenstates near a principal node is *double-valued*, namely the overall sign of both states is reversed if we increase $\phi \mapsto \phi + 2\pi$. Therefore, any *single-valued* gauge must necessarily exhibit a discontinuity – the Dirac string – across which both principal states flip sign. Each principal node must constitute the end-point of a Dirac string. Furthermore, since away from band nodes the eigenstates basis is continuous, there are no other end-points for Dirac strings. Therefore, in the eigenstate basis there is a *one-to-one correspondence* between the principal nodes and the end-points of Dirac strings. From this perspective, the gauge transformation to the continuous basis, analyzed in Eqs. (48–51), can be understood as creation of a new Dirac string that *exactly compensates* the "physical" Dirac string present in the eigenstate basis. This exactly resolves the apparent paradox presented in Sec E.

The exact position of the Dirac strings (i.e. besides

their fixed end-points) is arbitrary, and should not have any bearing on physical observables. Indeed, we find that both Euler connection and Euler form are *continuous* at a Dirac string. This readily follows from the transformation rules presented in Sec. C, namely we see from Eqs. (25) and (28) that the sign-reversing gauge transformation $X = -\mathbb{1}$ leaves both $\mathrm{Eu}(\boldsymbol{k})$ and $\mathrm{a}(\boldsymbol{k})$ invariant. We conclude that the relation $\mathrm{Eu}(\boldsymbol{k}) = d\,\mathrm{a}(\boldsymbol{k})$ remains valid along Dirac strings, meaning that they are no obstructions for the use of Stokes' thorem. Therefore, the *only* obstructions for Stokes' theorem are the principal nodes themselves, since at their locations the derivatives of the principal eigenstates (and thus also the Euler connection and the Euler form) are not well defined, cf. Sec. E. We thus use Stokes' theorem to relate

$$2\pi\chi(\mathcal{D}) = \int_{\mathcal{D}} \mathrm{Eu} - \oint_{\partial\mathcal{D}} \mathrm{a} \tag{69}$$

$$= \sum_{\alpha} \left(\int_{\mathcal{D}^{\epsilon}_{\alpha}} \mathrm{Eu} - \oint_{\partial\mathcal{D}^{\epsilon}_{\alpha}} \mathrm{a} \right) \tag{70}$$

where the summation index α indicates the principal nodes inside the region $\mathcal{D}$, and $\mathcal{D}^{\epsilon}_{\alpha}$ is a disc with radius ϵ centered at principal node α.

To simplify Eq. (70), we proceed as follows. First, we proved in Sec. E that Euler form is bounded near principal nodes, hence the integrals over $\mathcal{D}^{\epsilon}_{\alpha}$ converge to 0 in the limit $\epsilon \to 0$. Furthermore, it follows from Eq. (59) that $\mathbf{a} \cdot d\boldsymbol{\kappa} = \mp\frac{1}{2}\zeta d\phi$ for $\epsilon \to 0$, which integrates to $\mp\zeta\pi$ on $\partial\mathcal{D}^{\epsilon}_{\alpha}$. Plugging this result into Eq. (70), we find

$$\chi(\mathcal{D}) = \frac{\zeta}{2} \sum_{\alpha} w_{\alpha} \tag{71}$$

where $w_{\alpha} = \pm 1$ describes the *winding number* of the principal node, while $\zeta = \pm 1$ is the global orientation of the vector bundle. The result in Eq. (71) proves that $\chi(\mathcal{D})$ of the orientable bundle spanned by the two principal states on region $\mathcal{D}$ with a boundary is a *half-integer topological invariant* if one works in the eigenstate basis.

Let us conclude the section with several remarks:

1. Note that Eq. (71) expresses $\chi(\mathcal{D})$ as a sum of $\pm\frac{1}{2}$ quanta carried by the principal nodes. If the nodes were able to annihilate inside $\mathcal{D}$, then we would be left with a nodeless region, for which we proved in Eq. (68) that $\chi(\mathcal{D}) = 0$. Therefore, non-trivial value $\chi(\mathcal{D}) \neq 0$ is an obstruction for annihilating the principal nodes inside $\mathcal{D}$.

2. The two admissible values of a winding number $w_{\alpha} = \pm 1$ are reminiscent of the frame-rotation angle associated with the node being either $+\pi$ or $-\pi$. We prove in Sec. G that this intuition is correct, i.e. the two quantities are in an exact one-to-one correspondence.

3. One should take into account that Eq. (71) is not as useful in pratice as it appears! To make sure that we take the same orientation of the vector bundle at all principal nodes, it is necessary to know the bundle along some trajectories connecting the principal nodes. To avoid this extra work, our numerical algorithm for computing $\chi(\mathcal{D})$, presented in Sec. H is based on directly implementing Eq. (69).

4. In the presence of additional *adjacent* nodes, the vector bundle ceases to be orientable, and the relative orientation of two principal nodes depends on the specific choice of trajectory connecting them. This foreshadows the non-Abelian conversion of band nodes which we discuss in the main text of the manuscript. This "braiding" phenomenon is more carefully exposed in the next section.

G. Non-Abelian frame-rotation charge

In this section, we review the original derivation of the non-Abelian exchange of band nodes in $\boldsymbol{k}$-space, which was obtained by Ref. [18] using homotopy theory [28]. We subsequently show that the same non-Abelian behavior is reproduced by considering the Euler class on manifolds with a boundary, as has been defined in Sec. F. Similar observations on a less formal level were also made by Ref. [35]. The exact correspondence between the two approaches provides a proof that the two distinct mathematical descriptions of the braiding phenomena (homotopy theory vs. cohomology classes) are two windows into the same underlying topological structure.

In the homotopic description, one begins with identifying the space M_N of N-band real symmetric matrices that do not exhibit level degeneracy. This corresponds to Bloch Hamiltonians at momenta lying away from band nodes. With this assumption, we can uniquely order *all* eigenstates of $H(\boldsymbol{k})$ according to increasing energy into an $\mathsf{O}(N)$ matrix $\{|u^a(\boldsymbol{k})\rangle\}_{a=1}^{N} \equiv F(\boldsymbol{k})$, which can be interpreted as a an *orthonormal N-frame*. We further adjust band energies $\{\varepsilon^a(\boldsymbol{k})\}_{a=1}^{N}$ to some standard values (*e.g.* $\varepsilon^a = a$) while preserving their ordering. The space of such *spectrally normalized* Hamiltonians is $M_N = \mathsf{O}(N)/\mathbb{Z}_2^N$, where the quotient corresponds to flipping the overall sign of any of the N eigenvectors, which leaves the spectrally normalized Hamiltonian $H(\boldsymbol{k}) = \sum_{a=1}^{N} |u^a(\boldsymbol{k})\rangle\, \varepsilon^a\, \langle u^a(\boldsymbol{k})|$ invariant. Band nodes correspond to obstructions for a unique ordering of bands by energy, and thus induce discontinuities of frame $F(\boldsymbol{k})$.

To describe the band nodes, we study the topology of space M_N. Since there are 2^N different frames (corresponding to the quotient $\mathbb{Z}_2^N$) which all represent the same Hamiltonian, the following scenario is possible: We start at some point $\boldsymbol{k}_0$, and we follow the continuously rotating frame $F(\boldsymbol{k})$ that encodes the Hamiltonian $H(\boldsymbol{k})$ along $\boldsymbol{k} \in \gamma$, until we reach again $\boldsymbol{k}_0$ as the final point. Comparing the initial vs. the final frame at $\boldsymbol{k}_0$, we may find that they are two *different* of the 2^N frames representing the same Hamiltonian $\mathcal{H}(\boldsymbol{k}_0)$. We

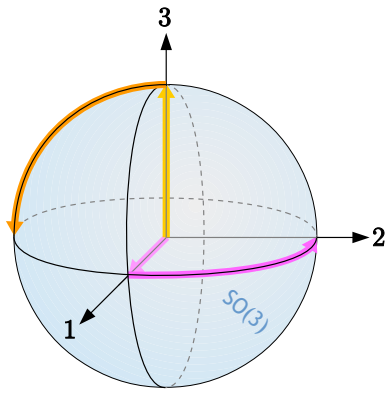

FIG. S-8. Geometry of rotations in three dimensions. If we represent clockwise rotation by angle $0 \leq \alpha \leq \frac{\pi}{2}$ around unit vector $\boldsymbol{n}$ by point with position $\boldsymbol{r} = \alpha\boldsymbol{n}$, then $\mathsf{SO}(3)$ looks like a ball with radius π and with antipodal points on the surface identified. The orange vs. the pink trajectory represent two ways of composing a π rotation around axis 1 with a π rotation around axis 3. The two trajectories cannot be continuously deformed into one another, i.e. they are topologically distinct. From this observation we deduce that topological charges associated with band nodes in consecutive band gaps do not commute with each other.

say that the Hamiltonian underwent a non-trivial *frame rotation*, which represents a non-trivial closed path inside M_N. For example, we know from Secs. E and F that a band node leads to a π-rotation of the frame by $X = (1, \ldots, 1, -1, -1, 1, \ldots, 1)$, where the two negative entries correspond to the two bands forming the node. More generally, since the handedness of the frame cannot change under the continuous evolution along γ, only $\frac{1}{2} \cdot 2^N = 2^{N-1}$ of the elements with $\det X = +1$ can actually be reached. Since the frame rotation is quantized to a discrete set of elements, it constitutes a topological invariant of the Hamiltonian $H(\boldsymbol{k})$ along path γ, which cannot change under continuous deformations as long as the spectrum along γ remains non-degenerate.

To explain the origin of the non-Abelian exchange of band nodes, let us briefly focus on models with $N = 3$ bands. The same discussion also applies to *any three consecutive bands* in models with $N \geq 3$ bands. A node formed by the lower (upper) two bands corresponds to a π-rotation in the first (last) two coordinates, i.e. $X_{12} = \mathrm{diag}(-1, -1, +1)$ [$X_{23} = \mathrm{diag}(+1, -1, -1)$]. A path that encloses *one of each* species of nodes is associated with total frame rotation $X_{13} = \mathrm{diag}(-1, +1, -1)$. However, while the geometric transformations

$$X_{12} \cdot X_{23} = X_{23} \cdot X_{12} \tag{72}$$

clearly commute, the continuous *paths* in $\mathsf{SO}(3)$ that realize the left-hand vs. the right-hand side of Eq. (72) are topologically *distinct*. To see this, recall that $\mathsf{SO}(3)$ can be visualized as a solid three-dimensional ball with radius π and with antipodal points on the surface being pairwise identified. This relation is achieved by mapping $R(\alpha; \boldsymbol{n})$ (i.e. a clockwise rotation by angle $0 \leq \alpha \leq \pi$ around axis given by unit vector $\boldsymbol{n}$), with a point inside the ball at position $\boldsymbol{r} = \alpha\boldsymbol{n}$. Then rotating first by π around axis 1 and then by π around axis 3 traces the pink path in Fig. S-8, while performing the two rotations in reverse order produces the orange path in Fig. S-8, which follows from

$$R(\alpha; \hat{\boldsymbol{e}}_3) \cdot R(\pi; \hat{\boldsymbol{e}}_1) = R(\pi; +\cos\tfrac{\alpha}{2}\hat{\boldsymbol{e}}_1 + \sin\tfrac{\alpha}{2}\hat{\boldsymbol{e}}_2) \tag{73}$$
$$R(\alpha; \hat{\boldsymbol{e}}_1) \cdot R(\pi; \hat{\boldsymbol{e}}_3) = R(\pi; +\cos\tfrac{\alpha}{2}\hat{\boldsymbol{e}}_3 - \sin\tfrac{\alpha}{2}\hat{\boldsymbol{e}}_2) \tag{74}$$

where $\hat{\boldsymbol{e}}_i$ indicates the unit vector directed along axis $i \in \{1, 2, 3\}$. The two paths in Fig. S-8 both connect the center of the ball to the π-rotation around axis 2. However, these paths cannot be continuously deformed into each other, i.e. they are topologically distinct. This ultimately follows from the fact that $\mathsf{SO}(3)$ is not a simply connected space. As a consequence, the ordering of the group elements from the $\mathbb{Z}_2^N$ quotient matters, and the topological charges associated with a pair of band nodes inside consecutive band gaps *do not commute*!

A careful analysis [18] reveals that the algebra of closed paths in space $M_N = \mathsf{O}(N)/\mathbb{Z}_2^N$ is governed by group Q_N (called "Salingaros group" [57]) which is uniquely characterized by the following four conditions [58]. We use $+1$ to indicate the identity element.

(*i*) There is a unique element $-1 \neq +1$ which has the property $(-1)^2 = +1$.

(*ii*) For each band gap $1 \leq G \leq (N-1)$ there is an associated element g_G such $(g_G)^2 = -1$.

(*iii*) $g_G \cdot g_{G'} = \epsilon g_{G'} \cdot g_G$, where $\epsilon = -1$ (anticommute) if $|G - G'| = 1$ and $\epsilon = +1$ (commute) otherwise.

(*iv*) All elements of Q_N can be expressed by composing elements g_G.

The element -1 corresponds to a 2π rotation (around any axis), and corresponds to the generator of the fundamental group $\pi_1[\mathsf{SO}(N)] = \mathbb{Z}_2$ [24]. Most interestingly, condition (*iii*) states that band nodes in consecutive band gaps carry *anticommuting charges*. This corresponds to the fact, visible in Fig. S-8, that

$$R(\pi, \hat{\boldsymbol{e}}_3) \cdot R(\pi, \hat{\boldsymbol{e}}_1) = \underbrace{R(2\pi, \hat{\boldsymbol{e}}_2)}_{\text{“}-1\text{”}} \cdot R(\pi, \hat{\boldsymbol{e}}_1) \cdot R(\pi, \hat{\boldsymbol{e}}_3) \tag{75}$$

if the rotations are interpreted as *paths* in $\mathsf{SO}(3)$. The group Q_3 coincides with the quaternion group $\{\pm 1, \pm \mathrm{i}, \pm \mathrm{j}, \pm \mathrm{k}\}$, therefore Q_N for $N \geq 3$ has been dubbed "generalized quaternions" by Ref. [18].

We finally show that the same anticommuting behaviour follows by studying the Euler form on manifolds with a boundary as defined in Sec. F. Our proof thus successfully bridges the homotopic description of Ref. [18] with the cohomological description proposed by Ref. [35] and further elaborated by the present work. To observe the non-trivial exchange, let us consider the situation, illustrated in Fig. S-9, with two principal nodes (blue dots)

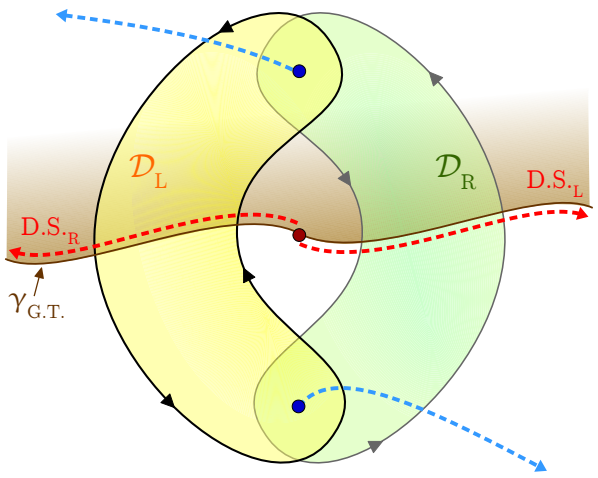

FIG. S-9. We consider two principal nodes (blue dots) near an adjacent node (red dot). Principal nodes are end-points of Dirac strings associated with a proper gauge transformation $X=-\mathbb{1}$ (dashed blue lines), which does not affect the continuity of Euler connection and Euler form of the vector bundle spanned by the two principal bands. On the other hand, the adjacent node is an end-point of a Dirac string associated with an improper transformation $X=\pm\sigma_z$ (dashed red line), which reverses the orientation of the bundle. The yellow resp. the green disc $\mathcal{D}_{\rm L,R}$ correspond to two topologically different coverings of the principal nodes, for which the bundle can be made orientable by choosing an appropriate position of the red Dirac string (indicated by D.S.$_{\rm L}$ resp. D.S.$_{\rm R}$). The two gauges are related by a gauge transformation which has an orientation-reversing discontinuity along $\gamma_{\rm G.T.}$ (solid brown line). This gauge transformation reverses the orientation of the bundle near one of the nodes, thus flipping the relative contribution of the two nodes to the sum in Eq. (71).

near an adjacent node (red dot). We know from Sec. F that principal nodes are end-points of Dirac strings carrying a proper gauge transformation $X=-\mathbb{1}$ on the two principal bands (dashed blue lines). We showed in the same section that such a gauge transformation is harmless for the calculation of the Euler class. On the other hand, adjacent nodes are end-points of Dirac strings carrying an *improper* gauge transformation $X=\pm\sigma_z$, which flips the sign of *just one* of the principal bands. Therefore, the bundle spanned by the two principal bands is non-orientable on regions containing such "adjacent" Dirac strings. Especially, an annulus enclosing the adjacent node is traversed by such a Dirac string for any single-valued gauge of the eigenstate basis, i.e. the bundle spanned by the principal bands is non-orientable on such an annulus.

Nevertheless, the total Euler class of the two principal nodes can still be calculated, provided that one covers the nodes with a disc lying to the side of the adjacent node. We show in Fig. S-9 two such discs, labelled $\mathcal{D}_{\rm L,R}$, which lie to the left (yellow) resp. to the right (green) of the adjacent node. Both discs admit a gauge with a well-defined orientation of the bundle, which is achieved by appropriately positioning the adjacent Dirac string (dashed red lines D.S.$_{\rm L}$ resp. D.S.$_{\rm R}$) such that it lies *outside* of the corresponding disc. Importantly, these two gauges are related by a gauge transformation that has a discontinuity along path $\gamma_{\rm G.T.}=$ D.S.$_{\rm L}\cup$ D.S.$_{\rm R}$ (solid brown path in Fig. S-9). This gauge transformation rotates D.S.$_{\rm L}$ into D.S.$_{\rm R}$ (and vice versa), and is simply equal to $X=\mathbb{1}$ on one side and to $X=\pm\sigma_z$ on the other side of the path $\gamma_{\rm G.T.}$. Such a gauge transformation necessarily reverses the orientation of the bundle at *exactly one* of the two principal nodes. It follows that the relative contribution of the two principal nodes to the sum in Eq. (71) is *reversed* due to the reversed orientation ζ near one of the nodes. Therefore, if the contributions of the two nodes to the Euler class cancel on $\mathcal{D}_{\rm L}$ [e.g. $\chi(\mathcal{D}_{\rm L})=\frac{1}{2}-\frac{1}{2}=0$], then the Euler class is automatically non-trivial on $\mathcal{D}_{\rm R}$ [corresponding to $\chi(\mathcal{D}_{\rm R})=\pm\left(\frac{1}{2}+\frac{1}{2}\right)=\pm1$]. Following the discussion at the end of Sec. F, the two principal nodes annihilate if brought together along a trajectory inside $\mathcal{D}_{\rm L}$, but are incapable to annihilate if brought together along a trajectory inside $\mathcal{D}_{\rm R}$. We thus conclude that the anticommutation relation in Eq. (75) [resp. in axiom (*iii*) on the previous page] is exactly reproduced by the behaviour of Euler class on manifolds with a boundary.

H. Numerical calculation of the Euler form.

To test the presented theory numerically, we have implemented a `Mathematica` code that takes as input (1) an N-band real-symmetric Bloch Hamiltonian, (2) two (consecutive) band indices, and (3) a rectangular region containing no adjacent nodes. The program outputs the Euler class on the defined region (with a boundary) for the selected pair of consecutive bands, by implementing Eq. (69) in the eigenstate basis. To work properly, the code also requires setting two hyper-parameters, which specify (*i*) the subdivison of the sides of the rectangular region into a discrete set of points, and (*ii*) a cut-off parameter which is used to regularize the numerical integration. The code is briefly described below, and we have made it available online [59].

The code sequentially implements the following steps. It begins by initializing the input parameters. We define a Bloch Hamiltonian `H[k1,k2]`, two (consecutive) band indices `LowerBand` and `UpperBand` that label the two principal bands, and a rectangular domain $k_1\in$ [`k1Min`, `k1Max`], $k_2\in$ [`k2Min`, `k2Max`]. The code automatically extracts the total number of bands `TotalBands`. The labelling of the bands is such that the lowest-energy band is indexed by `1`, and the highest-energy band is indexed by the value `TotalBands`. We further set the value of hyper-parameter `pts` which defines the discretization of the sides of the rectangular region into `pts` $\times$ `pts` infinitesimal squares of size `dk1` $\times$ `dk2`, where `dk1` $=$ (`k1Max` $-$ `k1Min`)/`pts` and similarly for `dk2`. We finally define hyper-parameter `cut` which is used later to regularize the numerical integration of Euler form.

In the next stage, we prepare the data for the numeri-

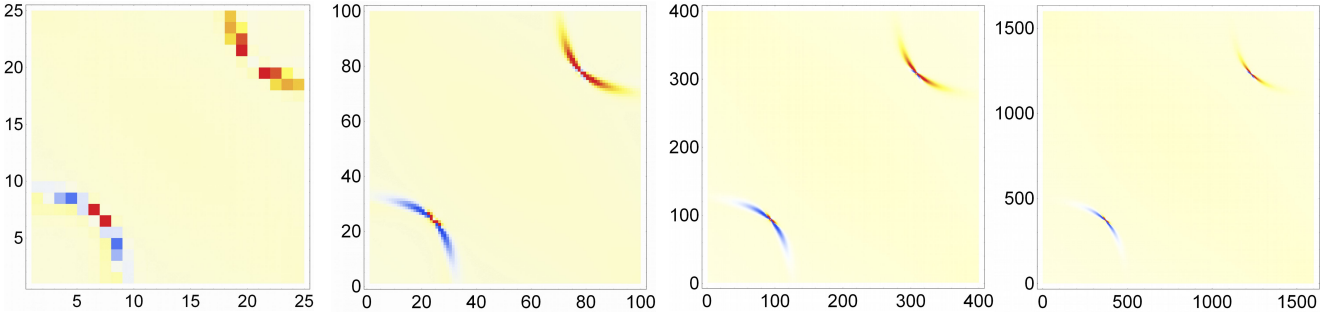

FIG. S-10. Numerically computed Euler form for the model in Eq. (1) of the main text for $t=-2.5$. The considered region $k_1 \in [-1,1]$ and $k_2 \in [-1,1]$ contains two principal nodes and no adjacent nodes. The four panels differ in the mesh size, $\texttt{pts} \in \{25, 100, 400, 1600\}$. The color scheme is logarithmic and identical for all the panels. It indicates negative (positive) values of $\mathrm{Eu}(\boldsymbol{k})$ with blue (red) tones, and saturates to blue (red) color for $\mp e^3 \approx 20$. We observe a divergent behavior of the Euler form near the principal nodes, which is an artifact of the numerical algorithm. Indeed, we find that the divergence shrinks to a smaller region near the nodes as we take a finer mesh `pts`. The light yellow background indicates that the Euler form is positive inside the region, with average value $\langle \mathrm{Eu} \rangle = (\int_{\mathcal{D}} \mathrm{Eu})/\mathrm{Area}(\mathcal{D}) \approx 0.25$. The detailed integration data are listed in the top part of Table I. The computed Euler class $\chi(\mathcal{D})=-1$ indicates that the two nodes cannot annihilate inside this region.

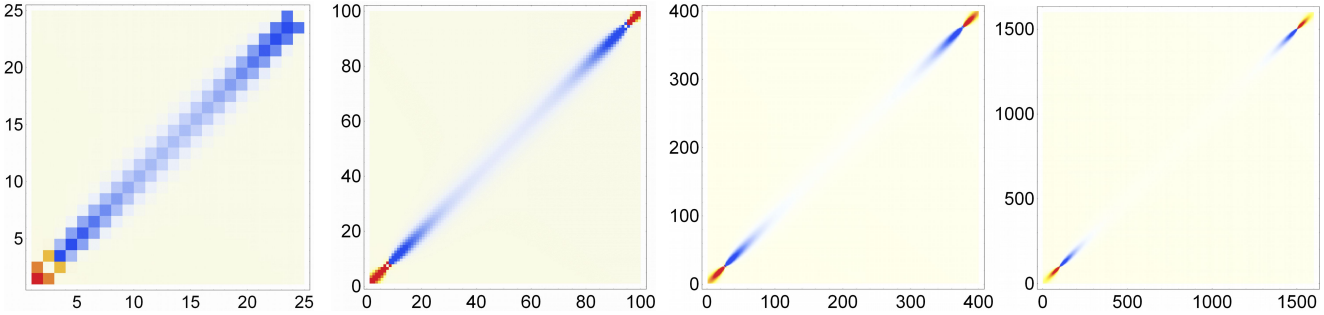

FIG. S-11. Data analogous to those shown in Fig. S-10, here obtained for model in Eq. (1) with $t=-5.5$ in region $k_1 \in [\pi-1, \pi+1]$ and $k_2 \in [\pi-1, \pi+1]$. The region contains two principal nodes. In fact, they are the same two nodes as in Fig. S-10, but as they occur at an earlier time t. The detailed integration data are listed in the bottom part of Table I. The computed Euler class $\chi(\mathcal{D})=0$ indicates that the two nodes are able to annihilate inside this region.

cal calculation of the derivatives that appear in the definition of Euler connection and Euler form. We save the two numerically obtained principal eigenstates of the Hamiltonian at the regular mesh of points into a $(\texttt{pts}+1)\times(\texttt{pts}+1)\times 2$ array called `AllStates`. Note that each entry of this array is itself an array of size $\texttt{TotalBands}\times 1$ (i.e. a right eigenstate). However, numerical diagonalization of the Hamiltonian finds the principal bands with a random $+/-$ gauge, which has to be smoothed before computing the derivatives. Furthermore, we know from Sec. F that each principal node is a source of a Dirac string associated with a $X=-\mathbb{1}$ gauge transformation. This implies the absence of a single-valued continuous gauge on regions containing principal nodes. To deal with these two issues, the code proceeds as follows. First, it computes the Berry phase on each of the $\texttt{pts}\times\texttt{pts}$ infinitesimal squares of the mesh, and stores the information in an array `Fluxes`. The default value is $+1$, while squares containing a node are indicated by value -1. Positions of all the nodes are then extracted and saved as pairs of numbers in array `Nodes`. Knowing the position of all the principal nodes inside the region, the code follows a set of rules to fix the position of the Dirac strings. The chosen trajectories of the Dirac strings are saved in array `Strings`. The infinitesimal squares traversed by a Dirac string are characterized by `Strings[[i,j]]=-1`, else the default value is `+1`. Finally, the two principal states are gauged such that they vary smoothly away from the Dirac strings, while both of the states simultaneously flip sign across each Dirac string. This gauge is then used to update all the states stored in array `AllStates`.

In the final stage, the code takes the gauged eigenstates saved in `AllStates`, and uses them to compute Euler form inside the region and Euler connection on the boundary of the region. Following Eq. (69), these two quantities are integrated to obtain the Euler class on the rectangular region. The integration of Euler connection along the boundary is straightforward, and the result is saved as `EulerConnectionIntegral`. On the other hand, more care is needed to correctly integrate the Euler form. The first complication has to do with calculating the Euler form on infinitesimal squares traversed by a Dirac string, where an extra gauge transformation is needed to compute the derivatives of the principal eigenstates. Note also that the code is set

to skip the computation of Euler form on infinitesimal squares containing the principal nodes (i.e. with `Fluxes[[i,j]]` $= -1$). The second problem is more subtle and relates to the analytic properties of Euler form near principal nodes in the eigenstate basis. Although we proved in Sec. E that $\mathrm{Eu}(\boldsymbol{k})$ is bounded and integrable near principal nodes, we observe that numerically calculated Euler form (saved in `pts` $\times$ `pts` array `EulerForm`) exhibits an oscillatory divergence near principal nodes [see the example data in Fig. S-10 and S-11]. The divergence is an artifact of the numerical computation of the derivatives (which we implement using the Euler method). More specifically, the computation fails in close vicinity of the nodes, since there the eigenstates change very rapidly on the scale of `dk1` and `dk2`, which are used in the numerical estimation of the derivatives. To regularize the numerical integration, we sum contributions to the Euler-form integral only over regions with $|$`EulerForm[[i,j]]`$| <$ `cut`. The obtained value of the integral is saved as `EulerFormIntegral`. We finally output `EulerClass`, which is the difference of `EulerFormIntegral` and `EulerConnectionIntegral` divided by 2π, cf. the definition in Eq. (69).

To demonstrate the performance of the code, we consider the model in Eq. (1) of the main text for $t = -2.5$, when the system exhibits two principal nodes near the *center* of the Brillouin zone. First, we consider in Fig. S-10 a square region $k_1 \in [-1, 1]$ and $k_2 \in [-1, 1]$, which contains the two principal nodes and no adjacent nodes. The numerically estimated values of the integrals of Euler connection and Euler form, together with the corresponding value of the Euler class, are listed in the top part of Table I. We find $\chi(\mathcal{D}) = -1$, which implies that the two principal nodes cannot annihilate. This prediction is indeed confirmed by panels $t \in \{-2, 0, +2\}$ in Fig. 2(a) of the main text, where we observe *bouncing* of the two principal nodes from the "dashed" to the "solid" diagonal of the Brillouin zone. In contrast, Fig. S-10 considers the same model but at an earlier time $t = -5.5$, when the same two principal nodes appear near the *corner* of the Brillouin zone. Considering the region $k_1 \in [\pi - 1, \pi + 1]$ and $k_2 \in [\pi - 1, \pi + 1]$, we find the Euler class to be trivial, $\chi(\mathcal{D}) = 0$. This implies that the two principal nodes *annihilate* if brought together along a trajectory inside this region, as is confirmed by decreasing the tuning parameter to $t \in \{-6, -10\}$ in Fig. 2(a) of the main text.

data in Fig. S-10			
`pts`	$\int_{\mathcal{D}} \mathrm{Eu}$	$\oint_{\partial\mathcal{D}} \mathrm{a}$	$\chi(\mathcal{D})$
25	1.1246	7.1618	−0.9609
100	0.9968	7.2546	−0.9960
400	0.9807	7.2608	−0.9995
1600	0.9779	7.2618	−1.0000
data in Fig. S-11			
`pts`	$\int_{\mathcal{D}} \mathrm{Eu}$	$\oint_{\partial\mathcal{D}} \mathrm{a}$	$\chi(\mathcal{D})$
25	−1.4565	0.0000	−0.2318
100	−0.5564	0.0000	−0.0886
400	−0.1766	0.0000	−0.0281
1600	−0.0504	0.0000	−0.0080

TABLE I. Integration data corresponding to the density plots of Euler form in Fig. S-10 resp. Fig. S-11, rounded to 10^{-4}. We find that the Euler class in the first setting converges to -1, and in the second setting to 0.

I. Critical nodes.

In three-dimensional models with $C_2\mathcal{T}$ symmetry, the non-Abelian frame-rotation charge may present an obstruction for the annihilation of two in-plane Weyl points with opposite chirality (process **D** in Fig. 5 of the main text). Especially, it is possible to bring two Weyl points of opposite chirality on top of each other by tuning Hamiltonian parameters. At that stage, a quadratic touching is realized, which we describe as a *stable critical node*. The node carries zero chirality, yet it cannot be gapped because of the non-Abelian topological charge. To study this phenomenon, we construct a two-band Hamiltonian that captures the two bands forming the stable critical point. We contrast the obtained model with the more conventional situation when we bring together Weyl points of opposite chirality and with a *trivial* frame-rotation charge (process **C** in Fig. 5 of the main text). We characterize the node formed by such two Weyl points at the moment of their annihilation as an *unstable critical node*. The present section contains derivation of the two models, while in the next Sec. J we discuss their Landau-level spectra presented in Fig. 6 of the main text.

We first study the case of opposite-chirality Weyl points with a *non-trivial* frame-rotation charge. We assume that the Weyl points are formed by the lower two out of the total of three bands. We begin with constructing the "stable critical Hamiltonian" $\mathcal{H}_{\mathrm{s.c.}}(\boldsymbol{k})$ inside the plane $k_z = 0$. We parameterize the in-plane momentum coordinates using the polar angle ϕ and the magnitude $k_\parallel = (k_x^2 + k_y^2)^{1/2}$ as $k_x = k_\parallel \cos\phi$ and $k_y = k_\parallel \sin\phi$. To get the non-trivial value 2π of the frame-rotation angle around the critical node, the eigenbasis frame must be rotated by an $\mathsf{SO}(3)$ matrix

$$R(\boldsymbol{k}) = \begin{pmatrix} \cos\phi & -\sin\phi & 0 \\ \sin\phi & \cos\phi & 0 \\ 0 & 0 & 1 \end{pmatrix}. \tag{76}$$

as we encircle the mpde. Assuming that the band energies near the point degeneracy inside the $k_z = 0$ plane depend only on the distance from the degeneracy, we write $E(k_\parallel) = \mathrm{diag}(-f(k_\parallel), +f(k_\parallel), 1)$, where the function $f(k_\parallel)$ will be determined later. We have further set the energy of the critical node to zero, and assumed that in the vicinity of the node the third band has energy $+1$.

The rotation matrix, together with the diagonal matrix

of band energies, lead to the in-plane Hamiltonian

$$\mathcal{H}_{\text{s.c.}}(k_\parallel,\phi) = R(\phi)\cdot E(k_\parallel)\cdot R^\top(\phi) = \begin{pmatrix} f(k_\parallel)\cos(2\phi) & f(k_\parallel)\sin(2\pi) & 0 \\ f(k_\parallel)\sin(2\pi) & -f(k_\parallel)\cos(2\pi) & 0 \\ 0 & 0 & +1 \end{pmatrix}. \quad (77)$$

With a bit of trigonometry, we find

$$\sin(2\phi) = \frac{2k_xk_y}{k_x^2+k_y^2} \quad \text{and} \quad \cos(2\phi) = \frac{k_x^2-k_y^2}{k_x^2+k_y^2}. \quad (78)$$

Since the Hamiltonian $\mathcal{H}_{\text{s.c.}}(\boldsymbol{k})$ should not be singular at $\boldsymbol{k}=\boldsymbol{0}$, we set $f(k_\parallel) = k_\parallel^2 = k_x^2+k_y^2$. The critical Hamiltonian inside the $k_z=0$ plane thus takes the form

$$\mathcal{H}_{\text{s.c.}}(k_x,k_y) = \begin{pmatrix} k_x^2-k_y^2 & 2k_xk_y \\ 2k_xk_y & -k_x^2+k_y^2 \end{pmatrix}. \quad (79)$$

where we have dropped the unimportant third band. Including a mass term $2m\sigma_x$ [or alternatively $2m\sigma_z$, but this just corresponds to the previous choice after rotating the (k_x,k_y) coordinates by $\pi/4$], we get the model

$$\mathcal{H}_{\text{bounce}}(k_x,k_y;m) = \begin{pmatrix} k_x^2-k_y^2 & 2k_xk_y+2m \\ 2k_xk_y+2m & -k_x^2+k_y^2 \end{pmatrix} \quad (80)$$

which exhibits two bouncing in-plane Weyl points nodes as m changes sign.

We finally need to complete the in-plane Hamiltonian to $k_z\neq 0$. First, note that the $C_{2z}\mathcal{T}$ symmetry, represented by $\mathcal{K}$, enforces the terms multiplying σ_y ($\sigma_{x,z}$) to be odd (even) in k_z. However, including the simplest possible term $k_z\sigma_y$ does *not* do the job, as that would produce two Weyl points with the *same* chirality. Especially, for $m=0$ one obtains the Hamiltonian of a double Weyl point [60]

$$\mathcal{H}_{\text{DWP}} = \Re[(k_x+\mathrm{i}k_y)^2]\sigma_z + \Im[(k_x+\mathrm{i}k_y)^2]\sigma_x + k_z\sigma_y \quad (81)$$

with total Chern number $|C|=2$. To instead get a model with $C=0$, we apply the following two steps. First, we replace $k_z\sigma_y \mapsto k_xk_z\sigma_y$ (or alternatively $k_yk_z\sigma_y$). This corrects the Chern number, but has a caveat, namely the resulting spectrum exhibits an accidental nodal line along $k_x=0=k_y$ for $m=0$. This final piece is amended by also including a term proportional to $k_z^2\sigma_x$ or $k_z^2\sigma_z$. We do the latter, leading to our final model

$$\mathcal{H}_-(\boldsymbol{k}) = 2(k_xk_y+m)\sigma_x + k_xk_z\sigma_y + (k_x^2-k_y^2-k_z^2)\sigma_z \quad (82)$$

The bouncing of Weyl points happens inside the $k_z=0$ plane. The two Weyl point are located at $k_x=k_y=\pm\sqrt{-m}$ for $m<0$, and at $k_x=-k_y=\pm\sqrt{m}$ for $m>0$. Focusing finally on the stable critical point node realized at $m=0$, we obtain

$$\mathcal{H}_{\text{s.c.}}(\boldsymbol{k}) = \begin{pmatrix} k_x^2-k_y^2-k_z^2 & 2k_x(k_y-\mathrm{i}k_z) \\ 2k_x(k_y+\mathrm{i}k_z) & -k_x^2+k_y^2+k_z^2 \end{pmatrix} \quad (83)$$

which disperses quadratically around $\boldsymbol{k}=\boldsymbol{0}$ in *all directions*. The stable critical node cannot be gapped as long as $C_{2z}\mathcal{T}$ symmetry is present. One can check that symmetry-compatible perturbations can at best split the critical node into a pair of Weyl points of opposite chirality. This remains true even if we couple the two-band model to additional bands at finite (non-zero) energy.

We now switch gears, and briefly compare the stable critical point to the case of two opposite-chirality in-plane Weyl points with a *trivial* frame-rotation charge. Such Weyl points are able to pairwise annihilate, and we describe the quadratic node at the moment of their annihilation as an *unstable critical node*. Repeating steps similar to those presented above, we arrive at a model

$$\mathcal{H}_+(\boldsymbol{k}) = 2(k_xk_y+m)\sigma_x + k_z\sigma_y + (k_x-k_y-k_z^2)\sigma_z \quad (84)$$

This model exhibits a pair of in-plane Weyl points located at $k_x=k_y=\pm\sqrt{-m}$ for $m<0$ (i.e. just as for the previous model), and *no* Weyl points for $m>0$. For $m=0$ we realize the *unstable* critical point, described by the Hamiltonian

$$\mathcal{H}_{\text{u.c.}}(\boldsymbol{k}) = \begin{pmatrix} k_x-k_y-k_z^2 & k_xk_y-\mathrm{i}k_z \\ k_xk_y+\mathrm{i}k_z & -k_x+k_y+k_z^2 \end{pmatrix} \quad (85)$$

which disperses quadratically inside the (k_x,k_y)-plane and linearly in the k_z direction. For the Hamiltonian $\mathcal{H}_+(\boldsymbol{k})$

J. Fingerprints of Euler class in Landau levels

We study Landau levels of Hamiltonians in Eqs. (82) and (84). Ignoring Zeeman coupling (we do not know the miscroscopic meaning of the two-level degree of freedom), this is achieved through the Peierls substitution. For a B-field along the z-axis, this ammounts to replacing

$$(k_x,k_y) \mapsto (-\mathrm{i}\partial_x + A_x, -\mathrm{i}\partial_y + A_y) \equiv (\Pi_x,\Pi_y) \quad (86)$$

while retaining k_z. In the last equation, we have explicitly set $\hbar=e=1$. Since the commutator $[\Pi_x,\Pi_y] = -\mathrm{i}(\partial_xA_y-\partial_yA_z) = -\mathrm{i}B$, we can conveniently express the Π-operators using the ladder operators $\mathfrak{a},\mathfrak{a}^\dagger$ (which fulfill $[\mathfrak{a},\mathfrak{a}^\dagger]=1$ and $[\mathfrak{a},\mathfrak{a}]=0=[\mathfrak{a}^\dagger,\mathfrak{a}^\dagger]$) as

$$\Pi_x = \sqrt{\frac{B}{2}}(\mathfrak{a}+\mathfrak{a}^\dagger) \quad \text{and} \quad \Pi_y = \mathrm{i}\sqrt{\frac{B}{2}}(\mathfrak{a}-\mathfrak{a}^\dagger). \quad (87)$$

Importantly, when representing quadratic terms such as k_xk_y using the ladder operators, we should be careful to retain Hermiticity. For example, the replacement

$$2k_xk_y \mapsto \mathrm{i}B(\mathfrak{a}+\mathfrak{a}^\dagger)(\mathfrak{a}-\mathfrak{a}^\dagger) = \mathrm{i}B\left[\left(\mathfrak{a}^2-\mathfrak{a}^{\dagger 2}\right) + \left(\mathfrak{a}^\dagger\mathfrak{a}-\mathfrak{a}\mathfrak{a}^\dagger\right)\right] \quad (88)$$

would *not be Hermitian*. The correct replacement requires us to first symmetrize the ordering of the momen-

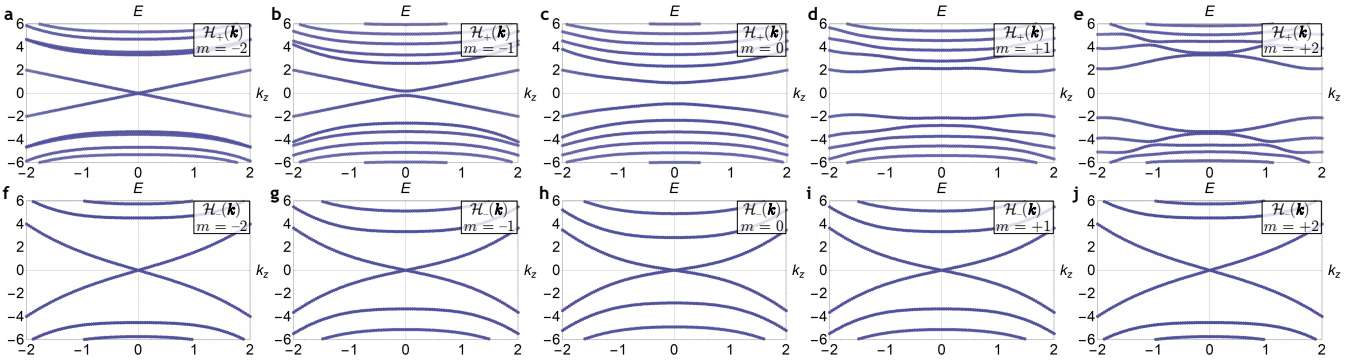

FIG. S-12. Landau levels of the model in Eq. (84) (top row) resp. in Eq. (82) (bottom row). The individual columns correspond to different values of the tuning parameter m. The two models exhibit a pair of Weyl points of opposite chirality at the same locations inside the momentum space for $m < 0$. In contrast, while the model in the top row is gapped for $m > 0$, the two Weyl points of the model in the bottom row remain present for $m > 0$ because of their non-trivial frame-rotation charge.

tum coordinates inside the polynomials,

$$k_x k_y + k_y k_x \mapsto \mathrm{i}\frac{B}{2}\left[(\mathfrak{a}+\mathfrak{a}^\dagger)(\mathfrak{a}-\mathfrak{a}^\dagger)+(\mathfrak{a}-\mathfrak{a}^\dagger)(\mathfrak{a}+\mathfrak{a}^\dagger)\right] = \mathrm{i}B\left(\mathfrak{a}^2-\mathfrak{a}^{\dagger 2}\right) \tag{89}$$

which is Hermitian. We similarly find that

$$k_x^2 - k_y^2 \mapsto B\left(\mathfrak{a}^2+\mathfrak{a}^{\dagger 2}\right). \tag{90}$$

In the numerics we also have to introduce cut-off on the dimension of the matrices representing ladder operators, which is known to induce non-physical states in the spectrum [12]. These "ghost states" can be identified by their large expectation value of the occupation number $\langle\psi|\,\hat{n}\,|\psi\rangle$, which grows without saturation upon increasing the cut-off.

We plot the numerically obtained Landau levels of the models in Eqs. (82) and (84) for $B = 1$ and for $m \in \{-2,-1,0,+1,+2\}$ in Fig. S-12. Let us first discuss the obersvations for the Hamiltonian $\mathcal{H}_+(\boldsymbol{k})$ with a *trivial* frame-rotation charge inside the $k_z = 0$ plane, which correspond to Fig. S-12**a**–**e**. We find that as the two Weyl points approach each other, their chiral Landau levels start to hybridize, leading to a large band gap $\Delta E \approx 2$ at the moment of their annihilation (i.e. for the unstable critical point at $m = 0$). In contrast, for the Hamiltonian $\mathcal{H}_-(\boldsymbol{k})$ with a *non-trivial* frame winding inside the $k_z = 0$ plane [38], we observe in Fig. S-12**f**–**j** a stable crossing of Landau levels at zero energy for all values of m. Such crossing, reminiscent of the Landau levels of a Dirac point, could thus serve as an experimental signature that two approaching in-plane Weyl points cannot annihilate.

The appearance of the zero-energy Landau level crossing of the Hamiltonian in Eq. (82) at $k_z = 0$ can be derived analytically. It amounts to showing that the equation $\mathcal{H}_-(k_x,k_y,0;m)\,|\psi\rangle = 0$ has two linearly independent solutions for all values of m. To get there, we first rewrite the Hamiltonian using the ladder operators, such that the equation for zero-energy states becomes

$$B\begin{pmatrix} \mathfrak{a}^2+\mathfrak{a}^{\dagger 2} & \mathrm{i}\left(\mathfrak{a}^2-\mathfrak{a}^{\dagger 2}\right)+\frac{2m}{B} \\ \mathrm{i}\left(\mathfrak{a}^2-\mathfrak{a}^{\dagger 2}\right)+\frac{2m}{B} & -\mathfrak{a}^2-\mathfrak{a}^{\dagger 2}\end{pmatrix}\begin{pmatrix}\sum_n c_n\,|n\rangle \\ \sum_n d_n\,|n\rangle\end{pmatrix} = \begin{pmatrix}0\\0\end{pmatrix} \tag{91}$$

where we decomposed both components of a zero-energy eigenstate using the number basis, with the property $\mathfrak{a}\,|n\rangle = \sqrt{n}\,|n-1\rangle$ and $\mathfrak{a}^\dagger\,|n\rangle = \sqrt{n-1}\,|n-1\rangle$. Finding a zero-energy eigenstate (if it exists) corresponds to finding a pair of sequences $\{c_n\}_{n=0}^\infty$ and $\{d_n\}_{n=0}^\infty$ that solve Eq. (91). Reading both rows of the equation corresponds to two sets of constraints, namely that $\forall n \in \mathbb{Z}_0^+$

$$(c_{n+2}+\mathrm{i}d_{n+2})\sqrt{(n+1)(n+2)} + (c_{n-2}-\mathrm{i}d_{n-2})\sqrt{n(n-1)} + \tfrac{2m}{B}d_n = 0 \tag{92}$$

$$(c_{n+2}+\mathrm{i}d_{n+2})\sqrt{(n+1)(n+2)} - (c_{n-2}-\mathrm{i}d_{n-2})\sqrt{n(n-1)} - \mathrm{i}\tfrac{2m}{B}c_n = 0. \tag{93}$$

For $n = 0$ and $n = 1$ the second term on the left-hand side of both equations vanishes, while the first term is the same for both equations. It therefore follows that

$$d_0 = -\mathrm{i}c_0 \qquad \text{and} \qquad d_1 = -\mathrm{i}c_1 \tag{94}$$

for any zero-energy eigenstate of the Landau-level Hamiltonian. For larger values of n, it is convenient to consider the sum and the difference of Eqs. (92) and (92)

$$\mathrm{i}(d_{n+2}-c_{n+2})\sqrt{(n+1)(n+2)}+\tfrac{m}{B}(d_n-\mathrm{i}c_n)=0 \quad (95)$$

$$-\mathrm{i}(d_n+\mathrm{i}c_n)\sqrt{n(n-1)}+\tfrac{m}{B}(d_{n+2}+\mathrm{i}c_{n+2})=0, \quad (96)$$

where in the second equation we relabelled $n \mapsto n+2$. The latter equation implies that if $d_n = -\mathrm{i}c_n$, the same relation also holds for $n+2$. Starting with Eqs. (94), we inductively find that $d_n = -\mathrm{i}c_n$ for all n. We insert this relation into Eq. (95), and find a simple recurrence relation

$$c_{n+2} = -\mathrm{i}\frac{m}{B}\frac{1}{\sqrt{(n+1)(n+2)}}c_n \quad (97)$$

with an arbitrary initial condition on c_0 and c_1. The solution to the recurrence is

$$c_{2\ell} = \left(-\frac{\mathrm{i}m}{B}\right)^{\ell}\frac{1}{\sqrt{(2\ell)!}}c_0 \quad (98)$$

$$c_{2\ell+1} = \left(-\frac{\mathrm{i}m}{B}\right)^{\ell}\frac{1}{\sqrt{(2\ell)!}}c_1. \quad (99)$$

We therefore conclude that there are two linearly independent zero-energy solutions to the Landau-level Hamiltonian at $k_z = 0$, which correspond to Eqs. (98-99) with initial conditions $c_0 = 1$ and $c_1 = 0$, resp. with $c_0 = 0$ and $c_1 = 1$ (and with $d_n = -\mathrm{i}c_n$ for both). Using finally that

$$\sum_{\ell=0}^{\infty}\left(\frac{m}{B}\right)^{2\ell}\frac{1}{(2\ell)!} = \cosh\left(\frac{m}{B}\right) \quad (100)$$

we obtain

$$|\psi^A\rangle = \frac{1}{\sqrt{\cosh\left(\frac{m}{B}\right)}}\sum_{\ell=0}^{\infty}\left(-\frac{\mathrm{i}m}{B}\right)^{\ell}\frac{1}{\sqrt{(2\ell)!}}\begin{pmatrix}|2\ell\rangle\\ -\mathrm{i}\,|2\ell\rangle\end{pmatrix} \quad (101)$$

$$|\psi^B\rangle = \frac{1}{\sqrt{\cosh\left(\frac{m}{B}\right)}}\sum_{\ell=0}^{\infty}\left(-\frac{\mathrm{i}m}{B}\right)^{\ell}\frac{1}{\sqrt{(2\ell)!}}\begin{pmatrix}|2\ell+1\rangle\\ -\mathrm{i}\,|2\ell+1\rangle\end{pmatrix} \quad (102)$$

as the two linearly independent zero-energy eigenstates normalized to unity.

[1] X.-G. Wen, Advances in Physics **44**, 405 (1995).
[2] M. Z. Hasan and C. L. Kane, Rev. Mod. Phys. **82**, 3045 (2010).
[3] X.-L. Qi and S.-C. Zhang, Rev. Mod. Phys. **83**, 1057 (2011).
[4] L. Fu and C. L. Kane, Phys. Rev. Lett. **100**, 096407 (2008).
[5] A. Kitaev (AIP, 2009) pp. 22–30.
[6] S. Ryu, A. P. Schnyder, A. Furusaki, and A. W. Ludwig, New Journal of Physics **12**, 065010 (2010).
[7] L. Fu, Phys. Rev. Lett. **106**, 106802 (2011).
[8] R.-J. Slager, A. Mesaros, V. Juričić, and J. Zaanen, Nature Physics **9**, 98 (2012).
[9] J. Kruthoff, J. de Boer, J. van Wezel, C. L. Kane, and R.-J. Slager, Phys. Rev. X **7**, 041069 (2017).
[10] R.-J. Slager, Journal of Physics and Chemistry of Solids **128**, 24 (2019), spin-Orbit Coupled Materials.
[11] X. Wan, A. M. Turner, A. Vishwanath, and S. Y. Savrasov, Phys. Rev. B **83**, 205101 (2011).
[12] T. Bzdušek, Q. Wu, A. Rüegg, M. Sigrist, and A. A. Soluyanov, Nature **538**, 75 (2016).
[13] H. C. Po, A. Vishwanath, and H. Watanabe, Nature Communications **8**, 50 (2017).
[14] J. Höller and A. Alexandradinata, Phys. Rev. B **98**, 024310 (2018).
[15] A. Bouhon, A. M. Black-Schaffer, and R.-J. Slager, arXiv preprint arXiv:1804.09719 (2018).
[16] B. Bradlyn, L. Elcoro, J. Cano, M. G. Vergniory, Z. Wang, C. Felser, M. I. Aroyo, and B. A. Bernevig, Nature **547**, 298 (2017).
[17] The Supplemental Material contains additional information about the (*a*) tight-binding models, (*b*) reality condition, (*c*) Euler form and Euler class, (*d*) their geometric interpretation in three-band models, (*e*) singularity of Euler form at principal nodes, (*f*) manifolds with boundary, (*g*) relation between Euler class and frame-rotation charge, (*h*) numerical algorithm, (*i*) critical nodes, and (*j*) Landau levels.
[18] Q. Wu, A. A. Soluyanov, and T. Bzdušek, ArXiv e-prints (2018), arXiv:1808.07469.
[19] J. Ahn, S. Park, D. Kim, Y. K. Kim, and B.-J. Y. Yang, ArXiv e-prints (2019), arXiv:1904.00336.
[20] J. Ahn, D. Kim, K. Youngkuk, and B.-J. Y. Yang, Phys. Rev. Lett. **121**, 106403 (2018).
[21] M. V. Berry, Proc. R. Soc. London, Se. A **392**, 45 (1984).
[22] J. Zak, Phys. Rev. Lett. **62**, 2747 (1989).
[23] Y. Zhang, Y.-W. Tan, H. L. Stormer, and P. Kim, Nature **438**, 201 (2005).
[24] G. K. Francis and L. H. Kauffman, Contemp. Math. **169**, 261 (1994).
[25] K. Liu, J. Nissinen, R.-J. Slager, K. Wu, and J. Zaanen, Phys. Rev. X **6**, 041025 (2016).
[26] T. Bzdušek and M. Sigrist, Phys. Rev. B **96**, 155105 (2017).
[27] N. D. Mermin, Rev. Mod. Phys. **51**, 591 (1979).
[28] M. Nakahara, *Geometry, Topology and Physics* (Taylor & Francis Group, Abingdon, 2003).
[29] V. Poenaru and G. Toulouse, J. Phys. Lett. **38**, 887 (1977).
[30] G. E. Volovik and V. P. Mineev, Zh. Eksp. Teor. Fiz **72**,

2256 (1977).
[31] L. A. Madsen, T. J. Dingemans, M. Nakata, and E. T. Samulski, Phys. Rev. Lett. **92**, 145505 (2004).
[32] G. P. Alexander, B. G.-g. Chen, E. A. Matsumoto, and R. D. Kamien, Rev. Mod. Phys. **84**, 497 (2012).
[33] Y. X. Zhao and Y. Lu, Phys. Rev. Lett. **118**, 056401 (2017).
[34] G. Walschap, *Metric Structures in Differential Geometry* (Springer-Verlag, New York, 2004).
[35] J. Ahn, S. Park, and B.-J. Yang, Phys. Rev. X **9**, 021013 (2019).
[36] A. Hatcher, "Vector Bundles and K-Theory," (unpublished).
[37] J. W. Milnor and J. D. Stasheff, Ann. Math. Stud. **76** (1975).
[38] X.-Q. Sun, S.-C. Zhang, and T. Bzdušek, Phys. Rev. Lett. **121**, 106402 (2018).
[39] A. A. Soluyanov, D. Gresch, Z. Wang, Q.-S. Wu, M. Troyer, X. Dai, and B. A. Bernevig, Nature **527**, 495 (2015).
[40] Z. Wang, D. Gresch, A. A. Soluyanov, W. Xie, S. Kushwaha, X. Dai, M. Troyer, R. J. Cava, and B. A. Bernevig, Phys. Rev. Lett. **117**, 056805 (2016).
[41] S.-Y. Xu, N. Alidoust, G. Chang, H. Lu, B. Singh, I. Belopolski, D. S. Sanchez, X. Zhang, G. Bian, H. Zheng, M.-A. Husanu, Y. Bian, S.-M. Huang, C.-H. Hsu, T.-R. Chang, H.-T. Jeng, A. Bansil, T. Neupert, V. N. Strocov, H. Lin, S. Jia, and M. Z. Hasan, Sci. Adv. **3** (2017), 10.1126/sciadv.1603266.
[42] T. Li, L. Duca, M. Reitter, F. Grusdt, E. Demler, M. Endres, M. Schleier-Smith, I. Bloch, and U. Schneider, Science **352**, 1094 (2016).
[43] F. Wilczek and A. Zee, Phys. Rev. Lett. **52**, 2111 (1984).
[44] N. Fläschner, B. S. Rem, M. Tarnowski, D. Vogel, D.-S. Lühmann, K. Sengstock, and C. Weitenberg, Science **352**, 1091 (2016).
[45] O. Zilberberg, S. Huang, J. Guglielmon, M. Wang, K. P. Chen, Y. E. Kraus, and M. C. Rechtsman, Nature **553**, 59 EP (2018).
[46] Y. Cao, V. Fatemi, S. Fang, K. Watanabe, T. Taniguchi, E. Kaxiras, and P. Jarillo-Herrero, Nature **556**, 43 EP (2018).
[47] H. C. Po, L. Zou, T. Senthil, and A. Vishwanath, Phys. Rev. B **99**, 195455 (2019).
[48] E. J. Sie, C. M. Nyby, C. Pemmaraju, S. J. Park, X. Shen, J. Yang, M. C. Hoffmann, B. Ofori-Okai, R. Li, A. H. Reid, *et al.*, Nature **565**, 61 (2019).
[49] D. B. Litvin, (International Union of Crystallography, 2013).
[50] C. J. Bradley and A. P. Cracknell, *The Mathematical Theory of Symmetry in Solids* (Oxford University Press, 1972).
[51] E. P. Wigner, Journal of Mathematical Physics **1**, 409 (1960).
[52] R. A. Horn and C. R. Johnson, *Matrix analysis* (Cambridge University Press, Cambridge, 2012).
[53] K. D. Ikramov, Comput. Math. Math. Phys. **52**, 1 (2012).
[54] H. A. Kramers, Koninkl. Ned. Akad. Wetenschap., Proc. **33**, 959 (1930).
[55] S.-s. Chern, Ann. Math. **46**, 674 (1945).
[56] A. Hatcher, *Algebraic Topology* (Cambridge University Press, Cambridge, 2002).
[57] N. Salingaros, J. Math. Phys. **25**, 738 (1983).
[58] A. Tiwari and T. Bzdušek, ArXiv e-prints (2019), arXiv:1903.00018.
[59] T. Bzdušek, "Euler class of a pair of energy bands on a manifold with a boundary," ResearchGate (2019), publicly available Mathematica code.
[60] C. Fang, M. J. Gilbert, X. Dai, and B. A. Bernevig, Phys. Rev. Lett. **108**, 266802 (2012).